A thesis submitted for the degree of Master of Science

Multi-photon Cross Section of Helium-like Ions Under Soft XUV Fields

Presented To:
The School of Physical Sciences
Dublin City University

Submitted By:
William Hanks B.Sc.

Supervisors:
Dr. Lampros Nikolopoulos
Prof. John Costello

SEPT 2017

I hereby certify that this material, which I now submit for assessment on the programme of study leading to the award of M.Sc. is entirely my own work, that I have exercised reasonable care to ensure that the work is original, and does not to the best of my knowledge breach any law of copyright, and has not been taken from the work of others save and to the extent that such work has been cited and acknowledged within the text of my work.

Signed: _____

Candidate ID No.: _____

Date: _____

Acknowledgements

First of all I would like to express my gratitude to my supervisor, Dr. Lampros Nikolopoulos, for his kindness in taking me on as a postgraduate student, and his continued supervision, guidance, and mentorship on this research project, as well as his efforts for the whole DAMOT (Dublin Atomic Molecular and Optical Theory) group at DCU.

Secondly, I would like to express my gratitude to my co-supervisor, Prof. John Costello, for his continued supervision and guidance on my research project as well as his efforts for the whole Laser Plasma Group at DCU.

I would also like to thank all the postgraduates, postdoctoral researchers and lecturers involved in DAMOT, the Laser Plasma Group at DCU, and the School of Physical Sciences in DCU who have helped me throughout my pursuits here, with their shared knowledge and friendship.

Contents

Abstract

William Hanks

Multi-photon Cross Section of Helium-like Ions Under Soft XUV Fields

One-, two- and three-photon l-partial ionization cross sections from the ground state of the following helium-like atoms/ions: He, Li^{+}, Ne^{8+} and Ar^{16+} are presented in this thesis. The expressions for the cross sections are based on the lowest-order perturbation theory for the electric field while the calculations are made with the use of an ab-initio code using a configuration-interaction method. Two-electron eigenstates are expanded on the corresponding one-electron eigenstate basis which are expressed as a set of nonorthogonal B-spline polynomials in a finite interval. The dipole matrix elements, used to compute the cross-sections, are calculated in two gauges: length and velocity, and they generally have good relative agreement granting the results a degree of confidence. It was found that cross sections are dominated by photo-resonance peaks as well as by peaks associated with two-electron excitation autoionizing resonances. It is observed that in the two-photon cross sections (in the non-resonant regions) the ^1D channel overwhelms the ^1S one. The general trend of decreasing cross sections with increasing atomic number (Z) of the target (i.e. from He to Ar^{16+}) is observed.

Chapter 1

Introduction

In this introductory chapter, a background of theoretical and experimental photoionization is presented. A quick overview of multiphoton absorption and ionization cross section definitions are given. A background of photoionization experimental advances is outlined, and examples of photon source facilities able to carry out such experiments are named. The modern feasibility of multiphoton ionization experiments and the motivation for this present theoretical work is conveyed.

1.1 Single- and Multi-photon Ionization

When an atom (or ion) is exposed to electromagnetic radiation, photo-absorption may occur: this can excite the atom to a bound state, or, if the photon energy is sufficiently high (surpassing the ionization potential of the atom) the atom can be excited to a continuum state, liberating the electron and causing ionization of the system. If the photon flux is sufficiently high, higher-photon absorptions can contribute significantly to ionization (e.g. two-photon absorption, requiring two photons to interact with the atom, is generally much less probable than single-photon absorption). These processes proceed through intermediate virtual states in the absence of a real resonance, and if the total-photon energy sum is above the ionization threshold, ionization can occur. Assuming the simplest multiphoton process,

two-photon absorption is a non-linear process and the probability is proportional to the square of the intensity. Accordingly, the probability of N-photo-absorption is proportional to the N-th power of the intensity [1] [2]. Any photoionization process need not absorb only the minimum number of photons to sum to the ionization potential − additional excess photons may be absorbed (a process known as "above threshold ionization"). See Figure 1.1 for a depiction of photoionization examples.

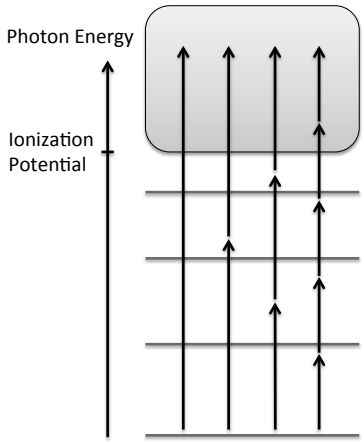

Figure 1.1: Diagram depicting, from left-to-right: single-photon ionization; two-photon ionization; three-photon ionization; and an example of above-threshold ionization (in this case a five-photon process with one excess photon). The shaded region represents the continuum.

The last three decades have produced a wealth of single-photoionization experiments, with the development of particle accelerators, particularly synchrotrons, capable of producing extreme ultraviolet (XUV) and x-ray beams. Here are some review articles detailing experimental processes of such [3] [4] [5].

Previously, photoionization experiments were limited to gases or vapours [6], but now positive (multiply charged) ion sources have been realized including electron-cyclotron-resonance (ECR) and electron beam ion traps (EBIT) [7]. Examples of facilities hosting such experiments include the Advanced Light Source (ALS) at Berkeley Lab, PETRA ("Positron-Elektron-Tandem-Ring-Anlage") at DESY ("Deutsches Elektronen-Synchrotron"), and ASTRID (Aarhus STorage RIng in Denmark) at Aarhus University [8] [9].

The existing photon ionization experiments call for additional modelling, especially for ion targets where data is lacking compared to neutral species, and especially in the XUV/VUV

(vacuum ultra violet) region where interesting, inner-shell processes occur, for example auto-ionization or Auger decay of the system.

More recently, during the last decade, the advent of new light sources producing high photon flux and/or ultrashort, coherent radiation, has renewed interest in both experimental and theoretical photoionization studies. Examples of these sources include: SACLA ("SPring-8 Angstrom Compact free electron LAser") in Japan; LCLS ("Linac Coherent Light Source") at SLAC ("Stanford Linear Accelerator Center") National Accelerator Laboratory; FLASH ("Free-Electron LASer in Hamburg") at DESY; and FERMI ("Free Electron laser Radiation for Multidisciplinary Investigations") in Italy [10] [11].

The high photon energy of these sources, produced either directly by free-electron lasers (FELs) or indirectly though high-harmonic generation techniques, can reach even to the soft- and hard-x-ray regimes. These high frequencies can probe more species for photon inner-shell processes, but also, the very short pulse durations enable fast processes at the natural time-scale of species to be examined, such as Auger processes [12], double core-hole creation and ionization [13] and on-resonance photoionization [14]. Additionally, the high intensity of these sources allows for unprecedented observations: two-photon ionization of helium (both single- and double-electron) [15]; full-stripping of neon [16]; and inner-shell multiphoton ionization of noble gases [17] [18]. Recent reviews have elaborated on this short wavelength regime [19, 20, 21, 22], and three new FELs are under development with enhanced laser pulse parameters: E-XFEL ("European X-ray FEL") in Hamburg, Swiss FEL in Switzerland and PAL XFEL ("Pohang Accelerator Laboratory X-ray FEL") in South Korea [10] [11].

The above discussion demonstrates the recent feasibility of inner-shell single- and multiphoton ionization experiments, and so there is now demand for modelling to complement experiment. While theoretical activity has increased since the late 2000s during the development of EUV/X-ray FELs, the theoretical description of multiphoton absorption and ionization requires the non-linear relationship of the X-ray radiation with the specific targeted species, especially ions to be treated.

This thesis addresses directly the non-linear relationship and applies it to produce one-,

two- and three-photon cross sections for a few helium-like species: He, Li^{+}, Ne^{8+} and Ar^{16+}, chosen for their experimental relevance (explained in the next chapter). This has been accomplished to fulfil the demand for theoretical modelling to complement experiment, to inspire further experiments, and to compare with the modelling of others, which is done throughout Chapter 3 (Results and Discussion). It is worth noting that other authors have been tackling related XUV photoionization problems, using other methods, for example those of the following papers [23] [24].

1.2 Units

In the presentation of the theoretical formulas, the Hartree atomic unit system is used, which sets the values of the following four constants to unity: $m_e = e = \hbar = \frac{1}{4\pi\epsilon_0} = 1$, where m_e is electron mass, e is elementary charge, $\hbar = \frac{h}{2\pi}$ is the reduced Planck's constant, h is Planck's constant and ϵ_0 is the permittivity of free space.

Elsewhere in this work, for example in tables, discussion text and plots, more traditional units are used, namely electronvolts (eV) for energy, and megabarns (Mb = 10^{-18} cm^2), cm^4s and cm^6s^2 for single-photon, two-photon and three-photon cross sections, respectively. These traditional units are used to better compare with experiment and other theoretical models, which both tend to use these units.

Chapter 2

Methods

In this chapter, the theoretical formulation and computational procedure used to ultimately produce the photoionization cross sections of He, Li^{+}, Ne^{8+} and Ar^{16+} is presented. The atomic structure of the chosen two-electron helium-like species and their one-electron ionizations (He^{+}, Li^{2+}, Ne^{9+} and Ar^{17+}) are presented in the form of their Hamiltonians, and the one-electron orbitals are solved though a separation of variables approach, numerically solved by an expansion of non-orthogonal B-spline polynomials limited to a finite atomic radius. The two-electron orbitals are then solved though an expansion of the one-electron solutions (the configuration interaction method). Finally, the cross section formulations, which are dependent on the dipole matrix elements, are presented, and the dipole matrix elements are expressed in two gauges (length and velocity). Additionally, basis parameters are stated and the performance of one run of the code for each two-electron and iconic one-electron species are tabulated and compared with the NIST atomic spectra database, with good agreement.

In this work, the one-, two- and three-photon cross sections of He, Li^{+}, Ne^{8+} and Ar^{16+} are addressed. To this end, an ab-initio configuration interaction method was chosen to represent the two-electron atomic structure. This particular method has been developed and described in detail over the years, and has been performed on He [25], Mg [26] and

Ca, and is one of the most reliable and robust methods in the case of two-electron systems. The rare gases He, Ne and Ar are often used in synchrotron or short wavelength FEL experiments due to their inertness and Li^+ has been used in one-photon experiments at the ALS [27]. Furthermore, this sample space of helium-like systems represents a reasonable range in atomic number while still remaining in the non-relativistic regime (see later).

2.1 Helium I, Lithium II, Neon IX, Argon XVII Atomic Structure

The Hamiltonian for He, Li^+, Ne^{8+} and Ar^{16+}, H_A, in atomic units, is given by:

$$H_A = \sum_{i=1}^{2} \left[-\frac{1}{2}\nabla_i^2 - \frac{Z}{r_i} \right] + \frac{1}{|\mathbf{r}_1 - \mathbf{r}_2|}, \tag{2.1}$$

where $\mathbf{r}_i$ is the coordinate of the i^{th} electron, r_i is the distance between the nucleus and the i^{th} electron, $-\frac{1}{2}\nabla_i^2$ represents the kinetic energy operator for the i^{th} electron, $-\frac{Z}{r_i}$ the Coulombic potential between the nucleus and the i^{th} electron, and $\frac{1}{|\mathbf{r}_1-\mathbf{r}_2|}$ represents the interelectronic Coulombic potential. The value for Z, the atomic number, is 2 for He, 3 for Li^+, 10 for Ne^{8+} and 18 for Ar^{16+}.

The computational procedure followed here has been presented in detail in a number of articles [28, 29, 30, 31, 32]. Briefly, the procedure to obtain the two-electron wavefunctions of He, Li^+, Ne^{8+} and Ar^{16+} is as follows:

Firstly, the Schrödinger equation (SE) is solved for He^+, Li^{2+}, Ne^{9+} and Ar^{17+}, adopting a separation of variables approach expressing the one-electron ionic orbitals as $\phi_{\varepsilon l m_l}(r) = (P_\varepsilon(r)/r)Y_{lm_l}(\theta,\phi)$, where the functions $Y_{lm}(\theta,\phi)$ are the well known spherical harmonics. Projection of $\phi_{\varepsilon lm}(r)$ onto the one-electron SE, followed by angular integration leads to the one-dimensional radial differential equation for the unknown radial orbitals, $P_\varepsilon(r)$:

$$\left[-\frac{1}{2}\frac{d^2}{dr^2} + \frac{1}{2}\frac{l(l+1)}{r^2} - \frac{Z}{r} - \varepsilon \right] P_\varepsilon(r) = 0, \tag{2.2}$$

where ε is the energy eigenvalue. This method models the radial space of the electron being limited to a finite radius (a "box size"), R, with the boundary conditions chosen so that the radial wavefunctions vanish at the boundaries of the box: $P_\varepsilon(0) = P_\varepsilon(R) = 0$. By doing this, it allows a formulation of a finite matrix representation of the physical Hamiltonian with a discretized eigenenergy spectrum, including both bound and continuum eigenstates, and expressing the bound states as negative valued while the continuum states are positive. The following discretized eigenevalue and eigenfunction notation is adopted to represent the discretized nature of the bound and even the continuum states: $\varepsilon \to \varepsilon_{nl}$ and $P_\varepsilon \to P_{nl}$. The negative energy states, $\varepsilon_{nl} < 0$, have an exponentially decaying asymptotic behaviour reflecting the bound spectrum, while the positive energy states, $\varepsilon_{nl} \geq 0$, have an oscillating asymptotic behaviour reflecting the continuum states. Note that the eigenenergies and the eignstates are dependent on the particular angular quantum number, l, according to Eq. (2.2). To numerically solve the above, the radial orbitals are expanded on a nonorthogonal set of B-spline polynomials [33] of order k_b and total number n_b defined in the finite interval $[0, R]$: $P_{nl} = \sum_{i=1}^{n_b} c_i^{(nl)} B_i^{(k_b)}(r)$ (note: in the case after the boundary conditions are considered and the first and last B-spline are removed, the summation occurs for $i = 2$ to $i = n_b - 1$). The choice of using a B-spline basis for the expansion (as opposed to, say, a Gaussian or Slater-type basis) is because of their strength in being able to represent both the bound and continuum natured solutions with great accuracy, and their ability to handle the boundaries. This expansion can be solved as a matrix diagonalization problem, with the solution providing the values of the unknown coefficients, $c_i^{(nl)}$.

Secondly, having produced the He^+, Li^{2+}, Ne^{9+} and Ar^{17+} one-electron radial eigenstates, $P_{nl}(r)$, for each partial wave $l = 0, 1, 2, ...$, the two-electron Schrödinger equation is then solved for He, Li^+, Ne^{8+} and Ar^{16+}:

$$H_A \Psi_{EL}(\mathbf{r}_1, \mathbf{r}_2) = E_L \Psi_{EL}(\mathbf{r}_1, \mathbf{r}_2). \tag{2.3}$$

This is achieved with a calculation method that is similar to how the one-electron solution was solved, although this time the two-electron eigenstates, Ψ_{EL}, are expanded on a set of

known two-electron functions (configuration basis), $\Phi_a^{(L)}(\mathbf{r}_1,\mathbf{r}_2)$:

$$\Psi_{EL}(\mathbf{r}_1,\mathbf{r}_2) = \sum_a C_a^{(EL)} \Phi_a^{(L)}(\mathbf{r}_1,\mathbf{r}_2), \tag{2.4}$$

where the goal is to express Eq. (2.3) as an algebraic equation of the $C_a^{(EL)}$ coefficients. This expansion is known as the configuration interaction (CI) method.

These configuration states are constituted by the eigenstates of the following operators: $\hat{H}_A^{(0)}$, $\mathbf{L}^2$, $\hat{L}_z$, $\mathbf{S}^2$, $\hat{S}_z$ and $\hat{\Pi}$ (parity), where $\hat{L} = \hat{l}_1 + \hat{l}_2$ and $\hat{S} = \hat{s}_1 + \hat{s}_2$. $\hat{l}_i$ and $\hat{s}_i$ are the angular and spin quantum numbers (respectively) of the i^{th} electron. $\hat{H}_A^{(0)}$ is the "zero order" two-electron Hamiltonian, which is equal to H_A of Eq. (2.1) less the $\frac{1}{|\mathbf{r}_1-\mathbf{r}_2|}$ term, i.e. it's the Hamiltonian of a fictional two-electron system where the electrons don't interact with each other. $\hat{L}$ is the total angular momentum operator, $\hat{L}_z$ is its projection onto the quantization axis, chosen to be the z-axis (the typical convention). $\hat{S}$ and $\hat{S}_z$ are the total spin operator and its projection onto the z-axis, respectively. It's assumed, according to the selection rules of the dipole approximation, and that only linearly polarized light is considered, that the light (field) interaction will not affect the total magnetic quantum number (M_L) or the total spin (S) or total magnetic spin quantum number (M_S) – these shall all remain as they were initially, and so, the CI states become only a function of their energy (E) and their total angular momentum quantum number (L). Since the other quantum numbers do not change, and two-electron systems are known to have a $^1S_0$ ground state, then only $M_L = 0$ and $S = 0$ states are involved in this photoionization process. As such, the zero-order states are fully described when the set of L and $a \equiv (n_1 l_1; n_2 l_2)$ in question is given. The respective zero-order energy is equal to $E_0 = \varepsilon_1 + \varepsilon_2$. Therefore the configuration basis set is composed of singlet ($S = 0$), spatially antisymmetric, angularly coupled, products of one-electron orbitals with $m_l = 0$:

$$\Phi^{(L)}_{n_1 l_1; n_2 l_2}(\mathbf{r}_1,\mathbf{r}_2) = C_{000}^{l_1 l_2 L} \hat{A}_{12} \left[\phi_{n_1 l_1}(\mathbf{r}_1)\phi_{n_2 l_2}(\mathbf{r}_2)\right] \tag{2.5}$$

where $\hat{A}_{12}$ is the antisymmetrization operator and $C_{000}^{l_1 l_2 L}$ the Clebsch-Gordan coefficent that ensures that the total magnetic quantum number and total spin are equal to $M_L = 0$, $S = 0$, respectively [34]. Projection of the above zero-order basis states onto Eq. (2.3) leads

to another matrix matrix diagonalization problem, with the solution this time providing the values of the CI energies, E, and the CI coefficients, $C_a^{(EL)}$ of Eq. (2.4). The physical interpretation of the coefficient is that the square of it, $|C_a^{(EL)}|^2$, represents the contribution of the (un-correlated) configuration, Φ_a^L (characterized by the set '$a = (n_1 l_1; n_2 l_2)$'), to the CI state, Ψ_{EL}, with energy E and angular momentum L.

Table 2.1: Electronic configurations included in the CI calculations for He, Li^+, Ne^{8+} and Ar^{16+}. Configurations in round brackets have been included for Li^+ but not for He, Ne^{8+} and Ar^{16+}; configurations in curly brackets have been included for Li^+, Ne^{8+} and Ar^{16+} but not for He.

^1S	^1P	^1D	^1F
s^2	sp	sd	sf
p^2	pd	p^2	pd
d^2	df	pf	pg
f^2	(fg)	d^2	df
$\{g^2\}$		dg	(fg)
		(f^2)	

2.1.1 Basis Parameters

B-splines are nonorthogonal polynomial functions that change definition at specific points called knots that make up a grid, and are used to generalise polynomial functions to approximate arbitrary functions. The knots may overlap, increasing the degree of polynomial definition change, and the grid may be one-dimensional. B-splines are used in this work for their ability to handle both bound and continuum states with accuracy. The order of B-splines used for the one-electron orbitals was $k_b = 9$ with the total number of B-spline polynomials being $n_b = 600$ for He^+, $n_b = 110$ for Li^{2+}, $n_b = 170$ for Ne^{9+} and $n_b = 170$ for Ar^{17+}, in a box varying between $R = 140 - 160$ a.u. for He^+, $R = 50 - 58$ a.u. for Li^{2+}, $R = 20 - 28$ a.u. for Ne^{9+} and $R = 10 - 14.8$ a.u. for Ar^{17+}. Calculations were carried out for many box-sizes, and these particular values were chosen for ultimately producing good cross section results, as seen later. The knot sequence for the B-spline basis was linear (meaning that the spacing between points where the B-spline polynomials change definition was constant), which was selected because both the bound states and continuum need to be well described. This was chosen as opposed to say, an exponential knot point distribu-

tion, because while the latter would describe the nucleus vicinity well it would do so at the expense of the continuum states. For the two-electron states of He, Li^+, Ne^{8+} and Ar^{16+}, in Table 2.1, information is given related to the CI basis used for the various symmetries $L = 0 - 3$. The two-electron wavefunctions, $\Phi_a^{(\Lambda)}(\mathbf{r}_1,\mathbf{r}_2)$, have been constructed from the zero-order configurations by one-electron orbitals with angular momenta as they are given in Table 2.1 and energies determined by the indices n_1, n_2 such as up to $1 \leq n_1 \leq 5$ and $1 \leq n_2 \leq 590$ for He, up to $1 \leq n_1 \leq 6$ and $1 \leq n_2 \leq 100$ for Li^+, up to $1 \leq n_1 \leq 5$ and $1 \leq n_2 \leq 160$ for Ne^{8+} and up to $1 \leq n_1 \leq 5$ and $1 \leq n_2 \leq 160$ for Ar^{16+} (also chosen, after many tests, for ultimately producing good cross sections). Note: these indices n_1, n_2 are not the principal quantum numbers, n_p, but rather the radial quantum numbers, n_r, related to the principal quantum number by: $n_p = n_r + l$ (where l is the angular momentum quantum number). Of course, the relation of the indices (n_1, n_2) with the energies of the zero-order wavefunctions depends on the basis size parameters such as the maximum value of the box radius as well as the number of B-spline basis used. This means that the maximum values of n_1, n_2 may vary in different calculations, depending on the parameters of the problem. Different symmetries are given different maximum n_1 orbital numbers, and, when not simply uniform, different configurations are given different maximum n_2 orbital numbers, with the trend of more being given to the configurations with the lowest n_1 orbital numbers, in particular with He, where the highest number of orbitals for n_2 was taken only for the configurations with an electron in the ground state. For example for the ^1S state the configuration $(n_1, l_1) = 1s$ has been combined with the $(n_2, l_2) = (2 - 591)p$ orbitals for He. For all their other combinations $(2s, 3s, 2p, ..)$, corresponding to excited states of the atomic system, a smaller number of (n_2, l_2) configurations was employed. For Li^+, however, a uniform max (n_2, l_2) number of 100 was used for all combinations, as was 160 for Ne^{8+} and Ar^{16+}. In summary, the whole basis, for each symmetry resulted in the inclusion of approximately 1390 configurations for He, approximately $1650 - 1940$ for Li^+ and approximately $2040 - 2360$ for Ne^{8+} and for Ar^{16+}, although only the lowest (in energy) 1300 configurations for He, the lowest 1100 for Li^+ and the lowest 1600 for Ne^{8+} and for Ar^{16+} were used to produce the data. These values were also chosen, after many tests, for ultimately producing good cross sections. The various computational parameters mentioned here for the one-electron orbitals and the two-electron configuration interactions have been

summarised in Table 2.2.

Table 2.2: Various computational parameters used in the one-electron orbital calculations for He^+, Li^{2+}, Ne^{9+} and Ar^{17+}, and in the two-electron CI calculations for He, Li^+, Ne^{8+} and Ar^{16+}.

	He^+	Li^{2+}	Ne^{9+}	Ar^{17+}
n_b	600	110	170	170
R (a.u.)	$140-160$	$50-58$	$20-28$	$10-14.8$
	He	Li^+	Ne^{8+}	Ar^{16+}
n_1	$1-5$	$1-6$	$1-5$	$1-5$
n_2	$1-590$	$1-100$	$1-160$	$1-160$
configurations:				
$\sim$ considered	1390	$1650-1940$	$2040-2360$	$2040-2360$
lowest included	1300	1100	1600	1600

2.1.2 Performance

Energies were able to be computed for the He^+, Li^2+, Ne^{9+} and Ar^{17+} one-electron states and the values obtained were in excellent agreement with those in the NIST atomic spectra database [35]: see Tables 2.3, 2.4, 2.5, 2.6 for the calculated lowest few S, P, D, F states and their comparisons with NIST. These tabulated data sets are from the lowest box-size R calculation for each species (140 $a.u.$, 50 $a.u.$, 20 $a.u.$, 10 $a.u.$, respectively), and note the results of each box-size R calculation were very similar for each species.

The He, Li^+, Ne^{8+} and Ar^{16+} two-electron states were reproduced with a small discrepancy from the current NIST values [35]: see Tables 2.7, 2.8, 2.9, 2.10 for the calculated lowest two S, P, D, F states, and lowest two energy differences from ground state, $\Delta E_1 = E(1s2p) - E(1s^2)$ and $\Delta E_2 = E(1s3p) - E(1s^2)$, and the NIST data to compare. Again note that these tabulated data sets are from the lowest box-size R calculation for each species, each having very similar results to the other box-size calculations of the same species. Note also the basis used to produce this calculated data includes the interelectronic potential.

All these energy values above are defined with respect to the double ionization threshold of He (which is the single ionization threshold of He^+), the double ionization threshold of

Li^+ (which is the single ionization threshold of Li^{2+}), the double ionization threshold of Ne^{8+} (which is the single ionization threshold of Ne^{9+}) and the double ionization threshold of Ar^{16+} (which is the single ionization threshold of Ar^{17+}). The values of the cross sections have been calculated with the use of the calculated energies.

Table 2.3: Lowest S, P, D, F energy states of the one-electron He^+ ion computed with a box-size R of 140 $a.u.$.

He^+	Calculated a.u.	Calculated eV	NIST eV	Discrepancy eV	Discrepancy %
$E(1s\ ^2S_{1/2})$	-2.00000	-54.4228	-54.4178	0.0050	0.009188
$E(2s\ ^2S_{1/2})$	-0.500000	-13.6057	-13.6047	0.0010	0.007350
$E(3s\ ^2S_{1/2})$	-0.222222	-6.04697	-6.04645	0.00052	0.008600
$E(4s\ ^2S_{1/2})$	-0.125000	-3.40142	-3.40109	0.00033	0.009703
$E(5s\ ^2S_{1/2})$	-0.0800000	-2.17691	-2.17668	0.00023	0.01057
$E(2p\ ^2P_{1/2})$	-0.500000	-13.6057	-13.6048	0.0009	0.006615
$E(3p\ ^2P_{1/2})$	-0.222222	-6.04697	-6.04647	0.00050	0.008269
$E(4p\ ^2P_{1/2})$	-0.125000	-3.40142	-3.40110	0.00032	0.009409
$E(5p\ ^2P_{1/2})$	-0.0800000	-2.17691	-2.17669	0.00022	0.01011
$E(3d\ ^2D_{3/2})$	-0.222222	-6.04697	-6.04626	0.00071	0.01174
$E(4d\ ^2D_{3/2})$	-0.125000	-3.40142	-3.40102	0.00040	0.01176
$E(5d\ ^2D_{3/2})$	-0.0800000	-2.17691	-2.17664	0.00027	0.01240
$E(4f\ ^2F_{5/2})$	-0.125000	-3.40142	-3.40099	0.00043	0.01264
$E(5f\ ^2F_{5/2})$	-0.0800000	-2.17691	-2.17663	0.00028	0.01286

By examining Tables 2.3, 2.4, 2.5, 2.6 it can be noticed that the one-electron ionic orbital ground states have the highest discrepancy with NIST and that the discrepancy decreases with increased state energy: this is because the ground state radial wavefunctions vary more rapidly in a tight region around the nucleus compared to the higher energy states, and so to describe them better a higher number of computational grid points is required around the nucleus. This could be solved by either having more B-splines (the number of B-splines is correlated with the number of computational grid points), but that would increase the computational cost of the code. Another solution would be to change the distribution of knot points, e.g. to an exponential distribution, but this photoionization study requires the continuum states to be defined well, so the liner distribution was kept. Additionally, decreasing the box-size would increase the density of computational grid points, but again this study requires a large box size to represent the continuum.

The two-electron states of Tables 2.7, 2.8, 2.9, 2.10 also have the same trend of dis-

Table 2.4: Lowest S, P, D, F energy states of the one-electron Li^{2+} ion computed with a box-size R of 50 $a.u.$.

Li^{2+}	Calculated a.u.	Calculated eV	NIST eV	Discrepancy eV	Discrepancy %
$E(1s\ ^2S_{1/2})$	-4.50000	-122.451	-122.454	0.003	0.002450
$E(2s\ ^2S_{1/2})$	-1.12500	-30.6128	-30.6148	0.0020	0.006533
$E(3s\ ^2S_{1/2})$	-0.500000	-13.6057	-13.6062	0.0005	0.003675
$E(4s\ ^2S_{1/2})$	-0.281250	-7.65320	-7.65331	0.00011	0.001437
$E(5s\ ^2S_{1/2})$	-0.180000	-4.89805	-4.89804	0.00001	0.0002042
$E(2p\ ^2P_{1/2})$	-1.12500	-30.6128	-30.6146	0.0018	0.005880
$E(3p\ ^2P_{1/2})$	-0.500000	-13.6057	-13.6063	0.0006	0.004410
$E(4p\ ^2P_{1/2})$	-0.281250	-7.65320	-7.65334	0.00014	0.001829
$E(5p\ ^2P_{1/2})$	-0.180000	-4.89805	-4.89806	0.00001	0.0002042
$E(3d\ ^2D_{3/2})$	-0.500000	-13.6057	-13.6052	0.0005	0.003675
$E(4d\ ^2D_{3/2})$	-0.281250	-7.65320	-7.65289	0.00031	0.004051
$E(5d\ ^2D_{3/2})$	-0.180000	-4.89805	-4.89782	0.00023	0.004696
$E(4f\ ^2F_{5/2})$	-0.281250	-7.65320	-7.65274	0.00046	0.006011
$E(5f\ ^2F_{5/2})$	-0.180000	-4.89805	-4.89775	0.00030	0.006125

Table 2.5: Lowest S, P, D, F energy states of the one-electron Ne^{9+} ion computed with a box-size R of 20 $a.u.$.

Ne^{9+}	Calculated a.u.	Calculated eV	NIST eV	Discrepancy eV	Discrepancy %
$E(1s\ ^2S_{1/2})$	-50.0000	-1360.57	-1362.20	1.63	0.1197
$E(2s\ ^2S_{1/2})$	-12.5000	-340.142	-340.681	0.539	0.1582
$E(3s\ ^2S_{1/2})$	-5.55556	-151.175	-151.366	0.191	0.1262
$E(4s\ ^2S_{1/2})$	-3.12500	-85.0356	-85.1234	0.0878	0.1031
$E(5s\ ^2S_{1/2})$	-2.00000	-54.4228	-54.4698	0.0470	0.08629
$E(2p\ ^2P_{1/2})$	-12.5000	-340.142	-340.701	0.559	0.1641
$E(3p\ ^2P_{1/2})$	-5.55556	-151.175	-151.373	0.189	0.1249
$E(4p\ ^2P_{1/2})$	-3.12500	-85.0356	-85.1260	0.0904	0.1062
$E(5p\ ^2P_{1/2})$	-2.00000	-54.4228	-54.4711	0.0483	0.08867
$E(3d\ ^2D_{3/2})$	-5.55556	-151.175	-151.238	0.063	0.04166
$E(4d\ ^2D_{3/2})$	-3.12500	-85.0356	-85.0692	0.0336	0.03950
$E(5d\ ^2D_{3/2})$	-2.00000	-54.4228	-54.4421	0.0193	0.03545
$E(4f\ ^2F_{5/2})$	-3.12500	-85.0356	-85.0503	0.0147	0.01728
$E(5f\ ^2F_{5/2})$	-2.00000	-54.4228	-54.4325	0.0097	0.01782

Table 2.6: Lowest S, P, D, F energy states of the one-electron Ar^{17+} ion computed with a box-size R of 10 $a.u.$.

Ar^{17+}	Calculated a.u.	Calculated eV	NIST eV	Discrepancy eV	Discrepancy %
$E(1s\ ^2S_{1/2})$	-162.000	-4408.24	-4426.22	17.98	0.4062
$E(2s\ ^2S_{1/2})$	-40.5000	-1102.06	-1107.89	5.83	0.5262
$E(3s\ ^2S_{1/2})$	-18.0000	-489.805	-491.882	2.077	0.4223
$E(4s\ ^2S_{1/2})$	-10.1250	-275.515	-276.465	0.950	0.3436
$E(5s\ ^2S_{1/2})$	-6.48000	-176.330	-176.838	0.505	0.2856
$E(2p\ ^2P_{1/2})$	-40.5000	-1102.06	-1108.04	5.98	0.5397
$E(3p\ ^2P_{1/2})$	-18.0000	-489.805	-491.930	2.125	0.4320
$E(4p\ ^2P_{1/2})$	-10.1250	-275.515	-276.485	0.970	0.3508
$E(5p\ ^2P_{1/2})$	-6.48000	-176.330	-176.848	0.518	0.2929
$E(3d\ ^2D_{3/2})$	-18.0000	-489.805	-490.505	0.700	0.1427
$E(4d\ ^2D_{3/2})$	-10.1250	-275.515	-275.884	0.369	0.1338
$E(5d\ ^2D_{3/2})$	-6.48000	-176.330	-176.541	0.221	0.1252
$E(4f\ ^2F_{5/2})$	-10.1250	-275.515	-275.685	0.170	0.06166
$E(5f\ ^2F_{5/2})$	-6.48000	-176.330	-176.439	0.109	0.06178

Table 2.7: Lowest S, P, D, F energy states, and lowest energy differences from ground state, of the two-electron He atom computed with a box-size R of 140 $a.u.$. $\Delta E_1 = E(1s2p\ ^1P_1) - E(1s^2\ ^1S_0)$ and $\Delta E_2 = E(1s3p\ ^1P_1) - E(1s^2\ ^1S_0)$.

He	Calculated a.u.	Calculated eV	NIST eV	Discrepancy eV	Discrepancy %
$E(1s^2\ ^1S_0)$	-2.88512	-78.5083	-79.0052	0.4969	0.6289
$E(1s2s\ ^1S_0)$	-2.14437	-58.3513	-58.3894	0.0381	0.06525
$E(1s3s\ ^1S_0)$	-2.06082	-56.0778	-56.0849	0.0071	0.01248
$E(1s4s\ ^1S_0)$	-2.03340	-55.3317	-55.3316	0.0001	0.0001807
$E(1s5s\ ^1S_0)$	-2.02108	-54.9965	-54.9940	0.0025	0.004546
$E(1s2p\ ^1P_1)$	-2.12341	-57.7809	-57.7871	0.0062	0.01073
$E(1s3p\ ^1P_1)$	-2.05500	-55.9194	-55.9181	0.0013	0.002325
$E(1s4p\ ^1P_1)$	-2.03100	-55.2665	-55.2631	0.0034	0.006152
$E(1s5p\ ^1P_1)$	-2.01987	-54.9635	-54.9594	0.0041	0.007460
$E(1s3d\ ^1D_2)$	-2.05561	-55.9360	-55.9311	0.0049	0.008761
$E(1s4d\ ^1D_2)$	-2.03127	-55.2738	-55.2688	0.0050	0.009047
$E(1s5d\ ^1D_2)$	-2.02001	-54.9674	-54.9624	0.0050	0.009097
$E(1s4f\ ^1F_3)$	-2.03125	-55.2733	-55.2681	0.0052	0.009409
$E(1s5f\ ^1F_3)$	-2.02000	-54.9671	-54.9620	0.0051	0.009279
ΔE_1	0.761714	20.7274	21.2180	0.4906	2.312
ΔE_2	0.830124	22.5889	23.0870	0.4981	2.157

Table 2.8: Lowest S, P, D, F energy states, and lowest energy differences from ground state, of the two-electron Li^+ ion computed with a box-size R of 50 *a.u.*. $\Delta E_1 = E(1s2p\ ^1P_1) - E(1s^2\ ^1S_0)$ and $\Delta E_2 = E(1s3p\ ^1P_1) - E(1s^2\ ^1S_0)$.

Li^+	Calculated a.u.	Calculated eV	NIST eV	Discrepancy eV	Discrepancy %
$E(1s^2\ ^1S_0)$	−7.25865	−197.518	−198.094	0.576	0.2908
$E(1s2s\ ^1S_0)$	−5.03817	−137.096	−137.172	0.076	0.05540
$E(1s3s\ ^1S_0)$	−4.73296	−128.790	−128.814	0.024	0.01863
$E(1s4s\ ^1S_0)$	−4.62945	−125.974	−125.985	0.011	0.008731
$E(1s5s\ ^1S_0)$	−4.58226	−124.690	−124.697	0.007	0.005614
$E(1s2p\ ^1P_1)$	−4.99219	−135.844	−135.878	0.034	0.02502
$E(1s3p\ ^1P_1)$	−4.71981	−128.433	−128.446	0.013	0.01012
$E(1s4p\ ^1P_1)$	−4.62398	−125.825	−125.832	0.007	0.005563
$E(1s5p\ ^1P_1)$	−4.57948	−124.614	−124.617	0.003	0.002407
$E(1s3d\ ^1D_2)$	−4.72236	−128.502	−128.505	0.003	0.002335
$E(1s4d\ ^1D_2)$	−4.62506	−125.854	−125.857	0.003	0.002384
$E(1s5d\ ^1D_2)$	−4.58003	−124.629	−124.632	0.003	0.002407
$E(1s4f\ ^1F_3)$	−4.62501	−125.853	−125.856	0.003	0.002384
$E(1s5f\ ^1F_3)$	−4.58001	−124.628	−124.631	0.003	0.002407
ΔE_1	2.26646	61.6736	62.2163	0.5427	0.8723
ΔE_2	2.53884	69.0853	69.6485	0.5632	0.8086

Table 2.9: Lowest S, P, D, F energy states, and lowest energy differences from ground state, of the two-electron Ne^{8+} ion computed with a box-size R of 20 *a.u.*. $\Delta E_1 = E(1s2p\ ^1P_1) - E(1s^2\ ^1S_0)$ and $\Delta E_2 = E(1s3p\ ^1P_1) - E(1s^2\ ^1S_0)$.

Ne^{8+}	Calculated a.u.	Calculated eV	NIST eV	Discrepancy eV	Discrepancy %
$E(1s^2\ ^1S_0)$	−93.8784	−2554.56	−2558.01	3.45	0.1349
$E(1s2s\ ^1S_0)$	−60.2901	−1640.58	−1642.67	2.09	0.1272
$E(1s3s\ ^1S_0)$	−54.5507	−1484.40	−1486.18	1.78	0.1198
$E(1s4s\ ^1S_0)$	−52.5529	−1430.04	−1431.73	1.69	0.1180
$E(1s5s\ ^1S_0)$	−51.6311	−1404.95	−1406.61	1.66	0.1180
$E(1s2p\ ^1P_1)$	−60.0519	−1634.10	−1635.99	1.89	0.1155
$E(1s3p\ ^1P_1)$	−54.4815	−1482.52	−1484.24	1.72	0.1159
$E(1s4p\ ^1P_1)$	−525.239	−1429.25	−1430.92	1.67	0.1167
$E(1s5p\ ^1P_1)$	−516.163	−1404.55	−1406.20	1.65	0.1173
$E(1s3d\ ^1D_2)$	−54.4997	−1483.01	−1484.01	1.00	0.06738
$E(1s4d\ ^1D_2)$	−52.5310	−1429.44	[no data]	[N/A]	[N/A]
$E(1s5d\ ^1D_2)$	−51.6199	−1404.65	[no data]	[N/A]	[N/A]
$E(1s4f\ ^1F_3)$	−52.5313	−1429.45	−1430.45	1.00	0.06991
$E(1s5f\ ^1F_3)$	−51.6200	−1404.65	−1405.65	1.00	0.07114
ΔE_1	33.8265	920.466	922.016	1.550	0.1681
ΔE_2	39.3969	1072.04	1073.77	1.73	0.1611

Table 2.10: Lowest S, P, D, F energy states, and lowest energy differences from ground state, of the two-electron Ar^{16+} ion computed with a box-size R of 10 $a.u.$. $\Delta E_1 = E(1s2p\ ^1P_1) - E(1s^2\ ^1S_0)$ and $\Delta E_2 = E(1s3p\ ^1P_1) - E(1s^2\ ^1S_0)$.

Ar^{16+}	Calculated a.u.	Calculated eV	NIST eV	Discrepancy eV	Discrepancy %
$E(1s^2\ ^1S_0)$	-312.878	-8513.84	-8546.89	33.05	0.3867
$E(1s2s\ ^1S_0)$	-198.435	-5399.71	-5422.37	22.66	0.4179
$E(1s3s\ ^1S_0)$	-178.153	-4847.79	-4867.43	19.64	0.4035
$E(1s4s\ ^1S_0)$	-171.073	-4655.14	-4673.86	18.72	0.4005
$E(1s5s\ ^1S_0)$	-167.802	-4566.11	-4584.48	18.37	0.4007
$E(1s2p\ ^1P_1)$	-197.973	-5387.13	-5407.31	20.18	0.3732
$E(1s3p\ ^1P_1)$	-178.019	-4844.14	-4863.04	18.90	0.3886
$E(1s4p\ ^1P_1)$	-171.017	-4653.61	-4672.00	18.39	0.3936
$E(1s5p\ ^1P_1)$	-167.773	-4565.34	-4583.54	18.20	0.3971
$E(1s3d\ ^1D_2)$	-178.054	-4845.10	-4863.30	18.20	0.3742
$E(1s4d\ ^1D_2)$	-171.030	-4653.96	-4672.13	18.17	0.3889
$E(1s5d\ ^1D_2)$	-167.780	-4565.52	-4583.59	18.07	0.3942
$E(1s4f\ ^1F_3)$	-171.031	-4654.00	[no data]	[N/A]	[N/A]
$E(1s5f\ ^1F_3)$	-167.780	-4565.53	[no data]	[N/A]	[N/A]
ΔE_1	114.905	3126.71	3139.58	12.87	0.4099
ΔE_2	134.859	3669.70	3683.85	14.15	0.3841

crepancies with NIST, except this time they are more extreme, especially at the ground state. While there would be a small contribution to error propagated from the one-electron states (at low atomic numbers, Z), the main error comes from the configuration interaction method, used to solve the $\frac{1}{|\mathbf{r}_1 - \mathbf{r}_2|}$ term. The reason why the error is smaller for the higher energy states is because the two-electrons have a lower influence on each other in the higher states (due to the lowering of the $\frac{1}{|\mathbf{r}_1 - \mathbf{r}_2|}$ term with the increase in distance between the electrons). The two-electron solutions could be improved by increasing the number of considered two-electron states in the configuration interaction, and if all states (an infinite number) were considered this would theoretically yield the exact solution.

2.2 Multiphoton Cross Section Formulation

According to the lowest-order perturbation theory, the N-photon L-partial ionization cross section, following the absorption of N photons of energy ω, from a system in its ground state, $|\Psi_g\rangle$ (of energy E_g), to a final continuum state of energy E and angular momentum L, is given by [32]:

$$\sigma_L^{(N)}(\omega) = 2\pi(2\pi\alpha)^N\omega^N|M_{E_L}^{(N)}(\omega)|^2 \tag{2.6}$$

where α is the fine structure constant and $M_{E_L}^{(N)}$ is the N-photon dipole matrix element (related to transition amplitude). The total N-photon cross section is obtained by summing up all the L-partial cross sections [32] [36]:

$$\sigma^{(N)}(\omega) = \sum_L \sigma_L^{(N)}(\omega) = 2\pi(2\pi\alpha)^N\omega^N \sum_L |M_{E_L}^{(N)}(\omega)|^2 \tag{2.7}$$

The N-photon dipole matrix element from an initial state $|\Psi_i\rangle$ to a final state $|\Psi_f\rangle$ is given by an N-fold summation over the whole spectrum of the allowed states [32] [37]:

$$M_{if}^{(N)} = \sum_{m_{N-1}} ... \sum_{m_1} \frac{\langle\Psi_i|V|\Psi_{m_1}\rangle\cdots\langle\Psi_{m_{N-1}}|V|\Psi_f\rangle}{\Delta\omega(m_1)\cdots\Delta\omega(m_{N-1})}, \tag{2.8}$$

where $\Delta\omega(m_j) = E_i + j\omega - E_{m_j}$ is the detuning, ω is the laser frequency and V is the atom-light (field) electric operator in the dipole approximation. $\langle\Psi_j|V|\Psi_{j'}\rangle$ is the two-electron ("effective single photon") dipole matrix element between the two states $|\Psi_j\rangle$ and $|\Psi_{j'}\rangle$, where Ψ is the two-electron CI eigenstate given by Eq. (2.4).

This study only considers the 1, 2 and 3 photon cases, and from the ground state, so the N-photon dipole matrix element formulae in the cases considered here reduces to the following:

$$M_{gf}^{(1)} = \langle\Psi_g|V|\Psi_f\rangle \tag{2.9}$$

$$M_{gf}^{(2)} = \sum_m \frac{\langle\Psi_g|V|\Psi_m\rangle\langle\Psi_m|V|\Psi_f\rangle}{E_i + \omega - E_m} \tag{2.10}$$

$$M_{gf}^{(3)} = \sum_{m_2}\sum_{m_1} \frac{\langle\Psi_g|V|\Psi_{m_1}\rangle\langle\Psi_{m_1}|V|\Psi_{m_2}\rangle\langle\Psi_{m_2}|V|\Psi_f\rangle}{[E_i + \omega - E_{m_1}][E_i + 2\omega - E_{m_2}]} \tag{2.11}$$

and note these summations sum over all bound and continuum states.

The dipole operator is computed with two gauges: the length form is $V = -\hat{\epsilon}_p \cdot (\mathbf{r}_1 + \mathbf{r}_2)$ and the velocity form is $V = \hat{\epsilon}_p \cdot (\nabla_1 + \nabla_2)/\omega$, where $\hat{\epsilon}$ is the polarization unit vector of the radiation [32].

In this study the dipole approximation is adopted when evaluating transition amplitudes, and while this is commonly accepted for low frequency light, where the wavelength of the light is much larger than the size of the atoms/ions, this study deals with light in the x-ray region (higher frequency) and so the use of the dipole approximation ought to be justified. It is done so by considering the scaling of the dipole transitions of one-electron systems, for which these calculations are carried out (see Eq (2.2)). The mean distance of the electron from the nucleus in the ground state, $\langle r \rangle$, scales with the atomic number, Z, as such: $\langle r(Z) \rangle = \frac{1}{Z}$, while the (one-electron) ionization potential, I_P, scales as: $I_P(Z) = Z^2$ (both in atomic units). For the considered (two-electron) two and three photon processes, the photon energy is less than the first (two-electron) ionization threshold (higher than that gets dominated by one-photon ionization): $\omega < |E(1s) - E(1s^2)|$, and since generally $|E(1s) - E(1s^2)| < I_P$, therefore $\omega < I_P$, which means $\omega < Z^2$. The dipole approximation requires that $|\mathbf{k}\cdot\mathbf{r}| << 1$, where $\mathbf{k}$ is the wavevector of the light and $\mathbf{r}$ is the electron's position − considering the scalar solution, and converting wavenumber (k) to photon energy, ω (in atomic units), this becomes: $\frac{\omega}{c}\langle r \rangle << 1$, where c is the speed of light. Earlier it was established that $\langle r \rangle = \frac{1}{Z}$, and taking $\omega = Z^2$ (the extreme of its previous inequality), the dipole approximation condition then becomes: $\frac{Z}{c} << 1$. In atomic units, $c \approx 137$, so $\frac{Z}{c} << 1$ is indeed true for $Z = 2, 3, 10, 18$, and so the dipole approximation is justified (and if $\omega < Z^2$ was taken, this would be even more true). This still leaves the one-photon cases with laser energies (exclusively) higher than the first (two-electron) ionization threshold: $\omega > |E(1s) - E(1s^2)|$. For these, taking the maximum energy values plotted for one-photon cross sections (see Figures 3.1, 3.2, 3.3, 3.4, in the next section) as ω, then $\frac{\omega}{c}\langle r \rangle$ becomes ≈ 0.008, ≈ 0.01, ≈ 0.05 and ≈ 0.1 for He^+, Li^{2+}, Ne^{9+} and Ar^{17+}, respectively, which satisfy the dipole approximation, but the higher Z ion calculations are expected to be less accurate, particularly for Ne^{8+} and (especially) Ar^{16+}.

For the single-photon ($N = 1$) case, the expression for the cross section is reduced to [38]:

$$\sigma_{if}^{(1)} = \frac{4\pi^2}{3c}(2L_f + 1)|M_{if}|^2\omega \tag{2.12}$$

where $L_f = L_i + 1$ (a single photon will change the angular momentum by 1). Since this study is concerned only with excitation from the ground state: $L_i = 0$ (S state), and so $L_f = 1$ (P state), which reduces the above to:

$$\sigma_{if}^{(1)} = \frac{4\pi^2}{c}|M_{gf}|^2\omega \tag{2.13}$$

In a two-photon process, the change in angular momentum due to the two photons can vector sum to $\Delta L = 0$ or $\Delta L = 2$, and since this modelling starts from the ground state with $L = 0$, the final state must be either $L = 0$ (S state) or $L = 2$ (D state) − as a result, the two-photon cross section in this case reduces to:

$$\sigma^{(2)} = \sum_{L=0,2} \sigma_L^{(2)} = 2\pi(2\pi\alpha)^2\omega^2 \sum_{L=0,2} |M_{E_L}^{(N)}|^2 \tag{2.14}$$

Similarly, since three photons may induce a change in orbital angular momentum $\Delta L = 1$ or $\Delta L = 3$, the final state must be either $L = 1$ (P state) or $L = 3$ (F state), reducing the three-photon cross section to:

$$\sigma^{(3)} = \sum_{L=1,3} \sigma_L^{(3)} = 2\pi(2\pi\alpha)^3\omega^3 \sum_{L=1,3} |M_{E_L}^{(3)}|^2. \tag{2.15}$$

Chapter 3

Results and Discussion

In this chapter, results for one-, two- and three-photon ionization cross sections are presented in the form of cross section plots and tables listing the occurrences of energy features for He, Li^+, Ne^{8+} and Ar^{16+}. The results are discussed, compared with each other to establish trends, and are compared with the theory and experimental data of other works, which are generally in good agreement.

Convinced about the reliability of the calculated electronic structure, within the available theoretical and experimental data to compare, it is now time to proceed to the main subject of this work: the presentation of ionization cross sections for a range of photon frequencies. In all of the following, the horizontal axes in the figures is the photon energy, in eV. The final angular momentum of the one-photon (He^+, Li^2+, Ne^{9+} and Ar^{17+}) absorption is the ^1P continuum, the angular momenta of the two-photon absorption are the ^1S,^1D continua, and the angular momenta of the three-photon absorption are the ^1P,^1F continua, all being of singlet symmetry. The results from the length and the velocity forms of the dipole operator have a small difference in logarithmic-scale plots, although larger differences may appear for near-resonant photon energies. Relative agreement between the length and the velocity forms is important since it is a strong evidence that the dipole matrix elements have been converged. Calculations were carried out for a wide range of atomic radii ("box sizes"), and multiple data sets were combined to form a single cross section plot. The particular cross section figures in this thesis (chosen for their good performance) have each been obtained

from calculations for 17 different radii, in between $140 - 160$ a.u. for He, $50 - 58$ a.u. for Li^+, $20 - 28$ a.u. for Ne^{8+} and $10 - 14.8$ a.u. for Ar^{16+}. The superposition of the zero order states produces an interference pattern in the cross sections, with often a single state dominating at an energy value forming a single peak due to that state, where the laser resonates with the state (or a transition state for multi-photon ionization), but sometimes a single state won't solely dominate and the interference pattern forms multiple peaks due to a superposition of some states. It is worth noting that the height (cross section value) of peaks doesn't have physical significance with the formulation used for this work, as these represent exact on-resonance cases and are theoretically infinite, and this could have been fixed if the inherent spontaneous decay width of intermediate bound states was accounted for.

3.1 Single-Photon Cross Section

Figures 3.1, 3.2, 3.3, 3.4 show the calculated one-photon cross sections of He, Li^+, Ne^{8+} and Ar^{16+} (respectively) from the ground state $1s^2(^1S_0)$ to $^1P_1$ states above the first ionization threshold. The final state in this case will be dominated by bound states and the free continuum $1s\varepsilon p(^1P_1)$. The results of both length and velocity gauge are plotted. The first data point in each of the four plots represents the ionization energy, and the single peak shown in each of the four plots corresponds to the $2s2p(^1P_1)$ two-electron excitation autoionizing resonance: Tables 3.1, 3.2, 3.3, 3.4 list the energy positions of these features and their comparisons with current NIST values [35].

3.1.1 Single-Photon Cross Section of He

Figure 3.1 displays a plot of photoionization cross section vs photon energy (of the light source) for He, with the first (most left) data point occurring at the ionization energy. A systematic reduction in cross section with increasing photon energy can be seen, except at the large peak, and after, the decreasing trend continues. The peak, occurring at 59.67 eV, is due to the $2s2p(^1P_1)$ doubly excited state of He. From Table 3.1 it is seen that there is

a discrepancy of ~ 0.5 eV between the established and computed ionization value, which is accounted for by the ground-state discrepancy listed in Table 2.7.

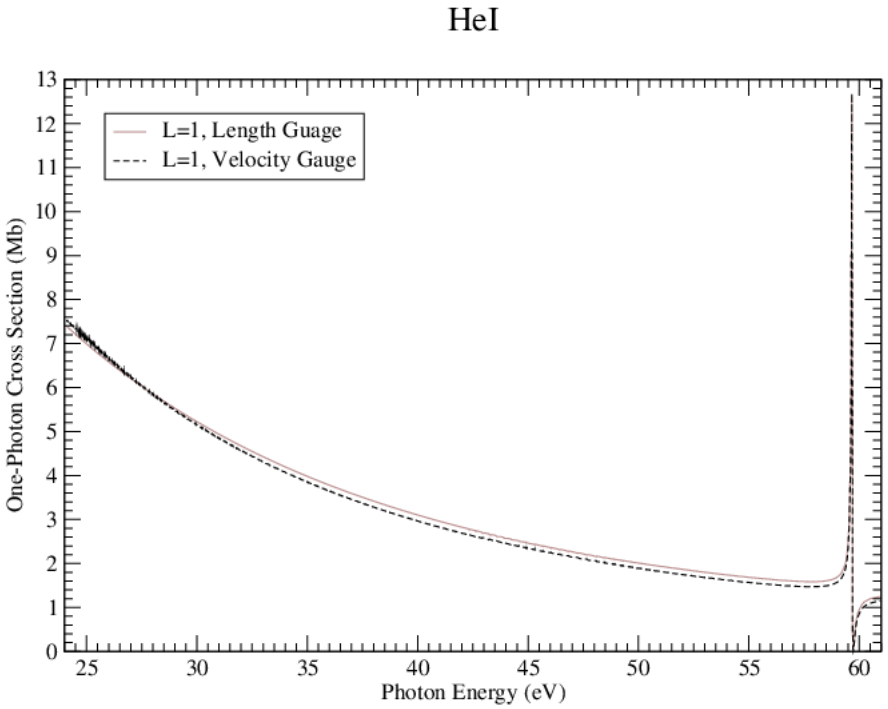

Figure 3.1: Single-photon ionization of He in the 24-61 eV region, with $n_b = 600$ B-splines of order $k_b = 9$, 17 box-sizes R varied between $140 - 160$ $a.u.$, and 1300 included orbital configurations.

Table 3.1: Energy features of He $\rightarrow$ He^+ one-photon ($L = 1$) cross section plot, compared to the currently accepted ionization energy and various energy levels.

	Calculated eV		NIST eV	Discrepancy eV	Discrepancy %
1^{st} Point	24.0726	Ionization	24.5874	0.5148	2.094
1^{st} Peak	59.6710	$2s2p(^1P_1)$	[no data]	[N/A]	[N/A]

Overall, the various non-resonant experimental data sets from West's study [39], ranging from $36.47-309.96$ eV ($340-40$ Å), agree well with Figure 3.1 ($24-61$ eV) outside the 59.67 eV resonance (which West's study avoided to only reflect the continuous cross section), and West's own tabulated data of that paper (starting from 504 Å (24.6 eV)) agrees very well with Figure 3.1, with all data points being within West's maximum error estimate of $\pm$ 5 % (except a point close to resonance, at 210 Å (59 eV)) and much of it (after 440 Å (28.2 eV) to before 210 Å) even within West's most probable error estimate of $\pm$ 3.5 %.

The cross section results of Chang and Tang's configuration interaction (using B-splines) method [30], on which this thesis's computational method is based, agree well with Figure 3.1 in their presented $\sim 0.1 - 0.9$ Ry[1] photoelectron region ($\sim 25.5 - 36.3$ eV photon energy region for Figure 3.1, when converted using the ionization energy of Table 3.1), and their $2s2p(^1P_1)$ resonance plot in their $35 - 36$ eV photoelectron energy region ($59.07 - 60.07$ eV photon energy region) is similar to the present work's in shape and position. Additionally, Figure 3.1, including its resonance, matches well in shape to the single-photon data presented in Nikolopoulos and Lambropoulos's work [25], who use a similar method to that of this thesis (though their cross section values are about half (off by $0.5 - 1$ Mb) that of Figure 3.1).

This good agreement of the He cross section with experiment and theory (using similar methods in which the present work is based) give validation in the method and its implementation for the work of this thesis, and grant confidence that the code shall work for the other two-electron species to be modelled.

3.1.2 Single-Photon Cross Section of Li^+

Figure 3.2 displays a plot of photoionization cross section vs photon energy for Li^+ with the first data point occurring at the ionization energy. As with He, what is seen is a systematic reduction except at a large peak due to the $2s2p(^1P_1)$ doubly excited state of Li^+. By looking at the y-axis scales, the cross section of Li^+ is noticeably lower (more than twice) than that of He. From Table 3.2 it is seen that there is a discrepancy of ~ 0.6 eV between the established and computed ionization and peak values, which is accounted for by the ground-state discrepancy listed in Table 2.8.

In the 135-155 eV region, the non-resonant data agrees well with the theoretical cross section for non-resonant photoionization of Verner *et al* [40], and agrees even better with the experimental data points in that region of the Advanced Light Source experiment of Scully *et al* [27] being within the systematic uncertainty error bars. However, in the region higher than 155 eV, it's harder to compare as Figure 3.2 has interference from other electron

[1] Ry, the Rydberg, is a unit of energy.

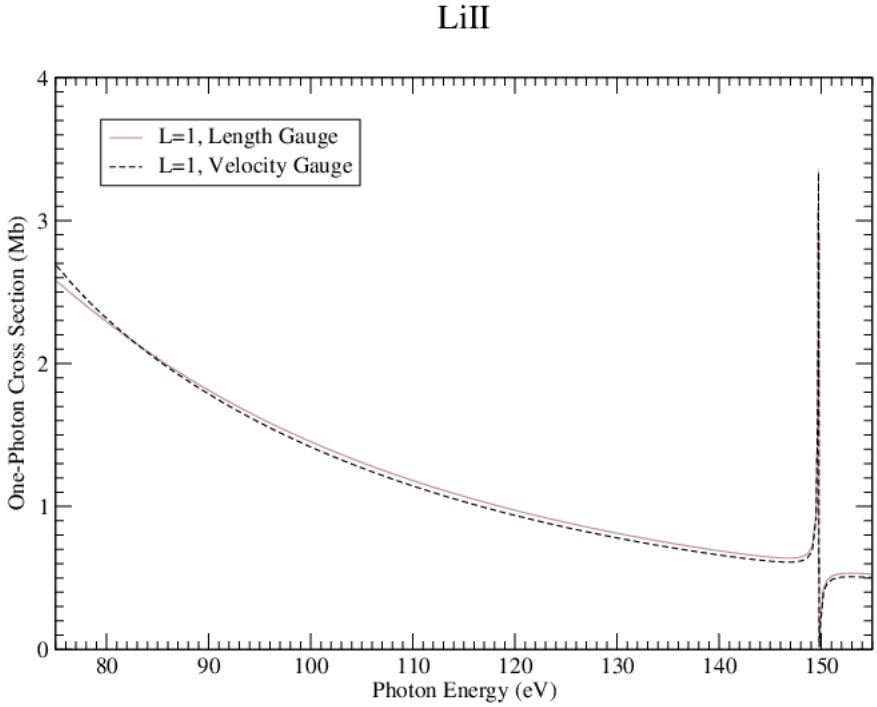

Figure 3.2: Single-photon ionization of Li^+ in the 75-155 eV region, with $n_b = 110$ B-splines of order $k_b = 9$, 17 box-sizes R varied between $50 - 58$ $a.u.$, and 1100 included orbital configurations.

Table 3.2: Energy features of $Li^+ \rightarrow Li^{2+}$ one-photon ($L = 1$) cross section plot, compared to the currently accepted ionization energy and various energy levels.

	Calculated eV		NIST eV	Discrepancy eV	Discrepancy %
1^{st} Point	75.0874	Ionization	75.6401	0.5527	0.7307
1^{st} Peak	149.738	$2s2p(^1P_1)$	150.289	0.551	0.3666

configuration states. The $2s2p(^1P_1)$ peak is of similar shape but is shifted down by approximately 0.6 eV compared to Scully *et al*'s experiment of that peak in the $149.5 - 151.0$ eV region (accounted for by the ground state discrepancy), and their theoretical cross sections have been convoluted with a Gaussian function to directly compare with their experiment.

3.1.3 Single-Photon Cross Section of Ne^{8+}

Figure 3.3 displays a plot of photoionization cross section vs photon energy for Ne^{8+}. It is similar to that of He and Li^+ in that there is generally a systematic reduction of cross

section except at a large peak (due to the $2s2p(^1P_1)$ doubly excited state of Ne^{8+}). However, a notable difference is a convex (-downward) behaviour at the start of the cross section plot (the low photon energy region). An additional difference is the scale, with the cross section of Ne^{8+} being an order of magnitude lower than He and Li^+ .

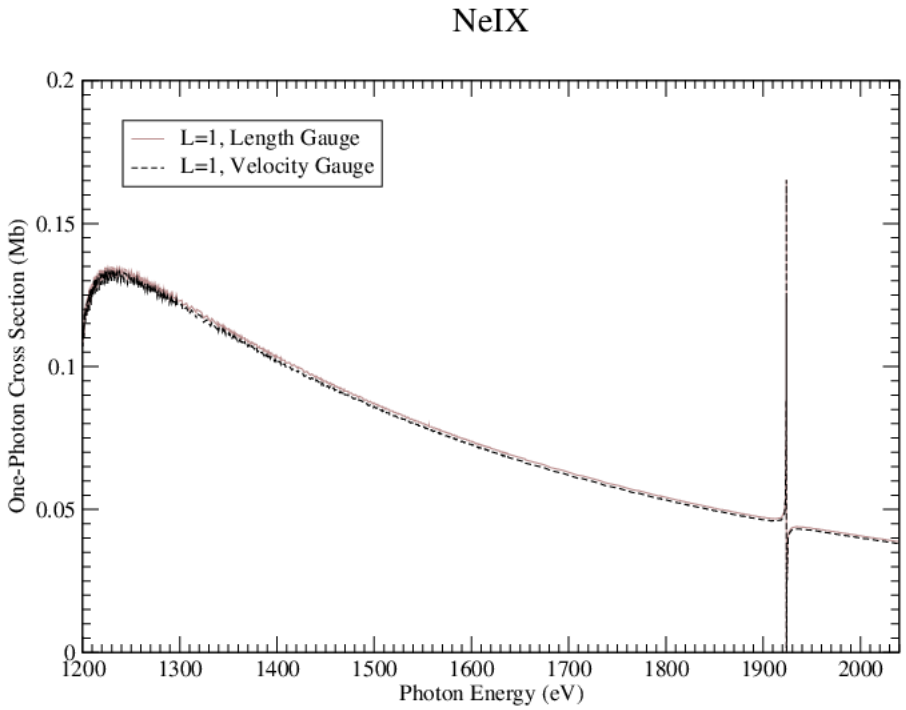

Figure 3.3: Single-photon ionization of Ne^{8+} in the 1200-2040 eV region, with $n_b = 170$ B-splines of order $k_b = 9$, 17 box-sizes R varied between $20 - 28$ $a.u.$, and 1600 included orbital configurations.

Table 3.3: Energy features of $Ne^{8+} \rightarrow Ne^{9+}$ one-photon ($L = 1$) cross section plot, compared to the currently accepted ionization energy and various energy levels.

	Calculated eV		NIST eV	Discrepancy eV	Discrepancy %
1^{st} Point	1194.17	Ionization	1195.81	1.64	0.1371
1^{st} Peak	1924.02	$2s2p(^1P_1)$	1926.63	2.61	0.1355

There are no known single-photon ionization cross section experimental data to date for Ne^{8+}. Bell and Kingston's photoionization cross section calculations [41] of Ne^{8+}, like all of their helium-like photoionization cross sections of that paper (including that of He and Li^+), keep rising towards the ionization energy (equivalently, zero ejected electron energy), indicating that the behaviour of the convex (-downward) region of Figure 3.3 may be non-

physical, and so an undetermined numerical error is suspected. One potential numerical error was tested for: that there were not enough oscillations of the electron wavefunction within the box length (which would break-down the box length sufficiently modelling the continuum), but this was ruled out by calculating the ratio of the box length with electron wavelength (at the convex (-downward) behaviour) for each of the four species (He, Li^{+}, Ne^{8+} and Ar^{16+}), and finding no obvious trend (e.g. of decreasing oscillations). Further investigation could conclude the undetermined nature of this region, however, since the primary focus of this work is on multiphoton ionization, this possible error does not affect the main body of this study.

From Table 3.3 it is seen that there is a discrepancy of ~ 1.6 eV between the established and computed ionization value, and a discrepancy of ~ 2.6 eV between the established and computed peak value − interestingly, these discrepancies are lower than the ground state discrepancy of ~ 3.5 eV (note that for He and Li^{+} they were about the same, and not less). One detail that might be related to this is the fact that the energy state discrepancies of Ne^{8+} (see Table 2.9) approach non-negligible values going down the table, while for He and Li^{+} (see Tables 2.7, 2.8) they approach negligible values, and this detail means that transitions, which are composed of differences in energies, will have their discrepancies shifted, in this case lowered. Alternatively (or perhaps the reason for the non-negligible higher-state discrepancies), an increase in the effect of relativistic effects with the higher atomic number of Ne^{8+} that wasn't accounted for could be causing the difference, or the use of the dipole approximation, which is less justified at this atomic number, could be causing the deviation. Furthermore, the odd behaviour of the cross section plot at the start, which suspected to be a numerical error, could be related to the lower than expected discrepancy of the ionization value. Another reason for the non-negligible higher-state discrepancies could be due to the increased weight of the one-electron calculation error compared to the two-electron calculation error introduced by the $\frac{1}{|\mathbf{r}_1-\mathbf{r}_2|}$ term, which is less significant against the $\frac{Z}{r_i}$ terms for the high Z of Ne^{8+}.

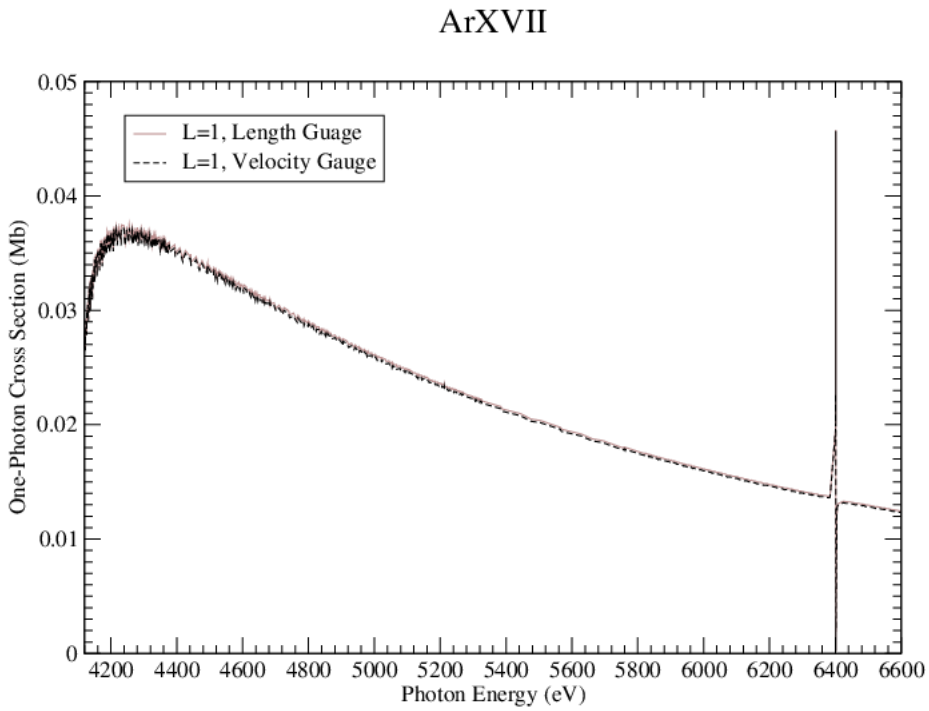

Figure 3.4: Single-photon ionization of Ar^{16+} in the 4120-6600 eV region, with $n_b = 170$ B-splines of order $k_b = 9$, 17 box-sizes R varied between $10 - 14.8$ $a.u.$, and 1600 included orbital configurations.

Table 3.4: Energy features of $Ar^{16+} \rightarrow Ar^{17+}$ one-photon ($L = 1$) cross section plot, compared to the currently accepted ionization energy and various energy levels.

	Calculated eV		NIST eV	Discrepancy eV	Discrepancy %
1^{st} Point	4106.72	Ionization	4120.67	13.95	0.3385
1^{st} Peak	6401.09	$2s2p(^1P_1)$	6426.00	24.91	0.3876

3.1.4 Single-Photon Cross Section of Ar^{16+}

Figure 3.4 displays a plot of photoionization cross section vs photon energy for Ar^{16+}. It is similar to the other species in that there is generally a systematic reduction of cross section except at a large peak (due to the $2s2p(^1P_1)$ doubly excited state of Ar^{16+}). However, it is notably different to He and Li^+ and similar to Ne^{8+} in that there is an odd curve at the start. Additional calculations could be done for a range of other helium-like ions of different atomic number, to see when this odd behaviour starts appearing, if it is in fact a feature of higher-Z species. Additionally, the scale is lower than the other three species, with the

cross section of Ar^{16+} being an order of magnitude less than Ne^{8+}.

From Table 3.4 it is seen that there is a discrepancy of ~ 14 eV between the established and computed ionization value, and a discrepancy of ~ 25 eV between the established and computed peak value − these discrepancies are lower than the ground state discrepancy of ~ 33 eV. Like with Ne^{8+}, these differences in expected discrepancies could be due to the non-negligible higher state discrepancies, an increase in the effect of relativistic effects, the use of the dipole approximation which is less justified at this atomic number, or the increased propagation of the one-electron state errors due to the high atomic number.

There are no known single-photon ionization cross section experimental data to date for Ar^{16+}.

3.2 Two-Photon Cross Section

Figures 3.5, 3.6, 3.7, 3.8, 3.9, 3.10, 3.11, 3.12 show the calculated two photon partial-ionization cross sections ($L = 0$, $L = 2$) of He, Li^+, Ne^{8+} and Ar^{16+} (respectively) from the ground state $1s^2(^1S_0)$ to $^1S_0$, $^1D_2$ states above the first ionization threshold. Total two-photon ionization cross section is obtained by the addition of all the L-partial cross sections of equation (2.7), but note these are logarithmic plots. The final state in this case will be dominated by bound states and the free $1s\varepsilon s(^1S_0)$ or $1s\varepsilon d(^1D_2)$ continua. The results of both length and velocity gauge are plotted. The two-photon cross sections are constituted by strong peak structures, which appear in both $L = 0$ and $L = 2$ symmetries, due to one-photon resonance with the intermediate states $1snp\,^1P_1$, $n = 2, 3, ...$, and there is interference (e.g. further peaks), which are unique to each symmetry ($L = 0, 2$), due to two-electron excitation autoionizing states of the type $npn'p$, $n, n' = 2, ...$, associated with the $^1S_0$, $^1D_2$ continua. Tables 3.5, 3.6, 3.7, 3.8, 3.9, 3.10, 3.11, 3.12 list the energy positions of various features of the cross sections, and their comparisons with current NIST values. The first data point in each represents half the ionization energy (of $He \rightarrow He^+$, $Li^+ \rightarrow Li^{2+}$, $Ne^{8+} \rightarrow Ne^{9+}$ and $Ar^{16+} \rightarrow Ar^{17+}$) (the established ionization energy is divided by two (two photons) to compare). The other entries are the positions of the highest points of

peaks, which are compared with various resonances, closely matching in value to currently established energy states. Each cross section was calculated up to the ionization energy of the respective species (any more than the ionization energy and single-photon ionization would dominate).

3.2.1 Two-Photon Cross Section of He

Figures 3.5 and 3.6 display plots of two-photon partial-ionization cross sections vs photon energy for He (for $L = 0$, and $L = 2$, respectively). The shape of the cross sections are quite different from the single-photon case, this time having strong peak structures due to resonance with intermediate $1snp\,^1P_1$, $n = 2, 3, ...$ states, and with large widths due to detuning (see the denominators of Eqs. (2.8), (2.10)), for example the wide peak feature with its highest point at 20.73 eV on the $L = 0$ cross section plot and 20.71 eV on the $L = 2$ plot, both represent the $1s2p\,^1P_1$ state. "E-notation" is used to express scientific notation for the interval marks on the y-axis, e.g. "1e-52" means "1×10^{-52}", and the scaling is remarkably lower, by many orders of magnitude, than the one-photon cross sections, but this is expected as the one-photon cases used the unit Mb = 10^{-18} cm^2, and two-photon cross sections are a product of two areas and a time duration (cm^{4}s), all having very small values (much less than 1), and so their product is an even smaller number. The non-resonant parts of the $L = 0$ partial cross section are about an order of magnitude lower than that of the $L = 2$ cross section.

From Tables 3.5, 3.6 it is seen that there is a discrepancy of ~ 0.3 eV between established and computed ionization values, and a discrepancy of ~ 0.5 - 0.6 eV between established and computed peak values − close to the ground state discrepancy of ~ 0.5 eV listed in Table 2.7.

When the partial cross section values are added up, and shifted by the ground state discrepancy of 0.50 eV, these results agree well with the (four) data points of Sato et al's experiment [42], being within the same order of magnitude, and agree even better (within 2 Mb) with two theoretical models Sato's paper compared with: R-matrix Floquet

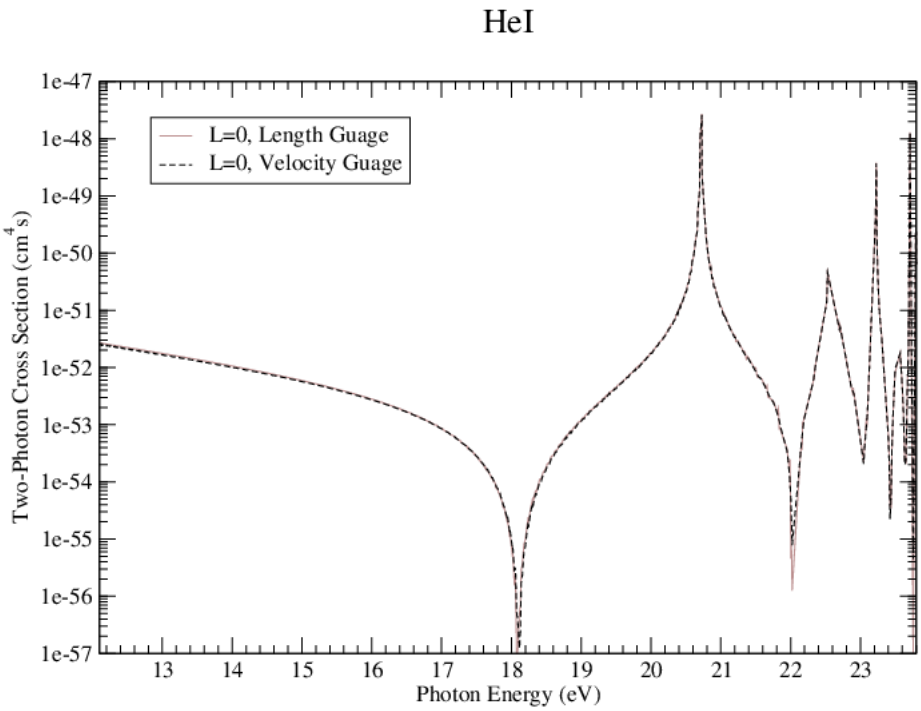

Figure 3.5: Two-photon, $L = 0$ ionization of He in the 12.1-23.8 eV region, with $n_b = 600$ B-splines of order $k_b = 9$, 17 box-sizes R varied between $140 - 160$ $a.u.$, and 1300 included orbital configurations.

Table 3.5: Energy features of He $\rightarrow$ He$^+$ two-photon, $L = 0$ cross section plot, compared to the currently accepted ionization energy and various energy levels.

	Calculated eV		NIST eV	Discrepancy eV	Discrepancy %
		Ionization	24.5874		
1$^{\text{st}}$ Point	12.0395	$\hookrightarrow \div 2$	12.2937	0.2542	2.068
1$^{\text{st}}$ Peak	20.7287	$1s2p(^1P_1)$	21.2180	0.4893	2.306
2$^{\text{nd}}$ Peak	22.5289	$1s3p(^1P_1)$	23.0870	0.5581	2.417
3$^{\text{rd}}$ Peak	23.2268	$1s4p(^1P_1)$	23.7421	0.5153	2.170
4$^{\text{th}}$ Peak	23.5690	$1s5p(^1P_1)$	24.0458	0.4768	1.983

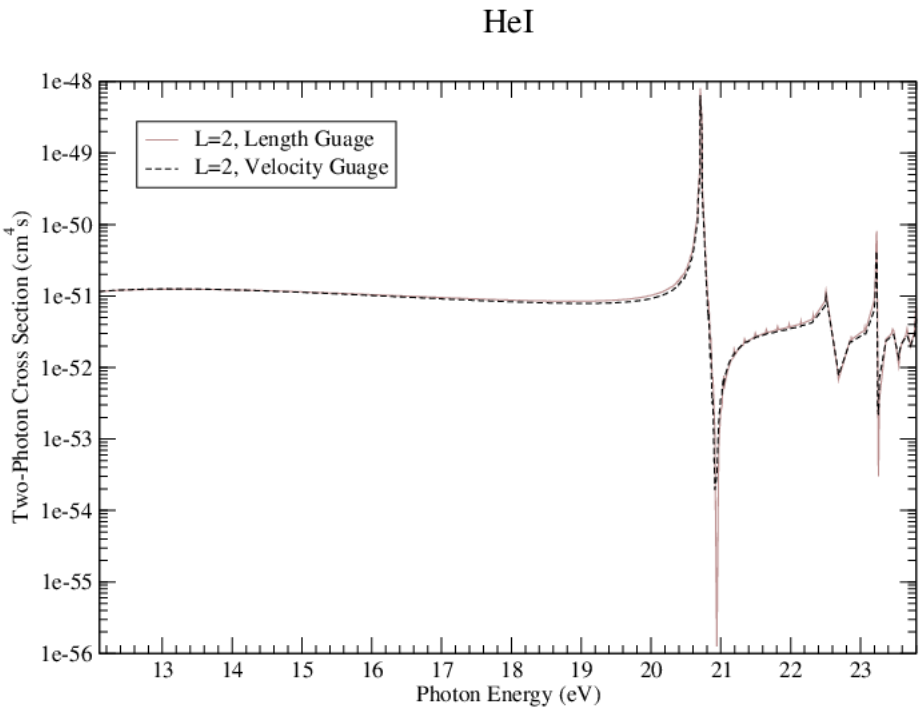

Figure 3.6: Two-photon, $L = 2$ ionization of He in the 12.1-23.8 eV region, with $n_b = 600$ B-splines of order $k_b = 9$, 17 box-sizes R varied between $140 - 160$ $a.u.$, and 1300 included orbital configurations.

Table 3.6: Energy features of He $\rightarrow$ He$^+$ two-photon, $L = 2$ cross section plot, compared to the currently accepted ionization energy and various energy levels.

	Calculated eV		NIST eV	Discrepancy eV	Discrepancy %
		Ionization	24.5874		
1$^{\text{st}}$ Point	12.0374	$\hookrightarrow \div 2$	12.2937	0.2563	2.085
1$^{\text{st}}$ Peak	20.7050	$1s2p(^1P_1)$	21.2180	0.5130	2.418
2$^{\text{nd}}$ Peak	22.5066	$1s3p(^1P_1)$	23.0870	0.5804	2.514
3$^{\text{rd}}$ Peak	23.2363	$1s4p(^1P_1)$	23.7421	0.5058	2.130
4$^{\text{th}}$ Peak	23.4607	$1s5p(^1P_1)$	24.0458	0.5851	2.433

method [43] and lowest-order perturbation theory [25].[1] When shifted by 0.50 eV, Figure 3.6 matches well in cross section values and shape, including resonances, with the $L = 2$ (D channel) cross section of [25] (note they used an atomic radius ("box size") of 40 a.u.).

Note: two-photon auto-ionizing state peaks from ^1S, ^1D terms would occur at higher energies, beyond about 29 eV (the lowest post-ionization energy levels are about 58 eV, and half that value (two photons) is about 29 eV).

3.2.2 Two-Photon Cross Section of Li^+

Figures 3.7 and 3.8 display plots of two-photon partial-ionization cross sections vs photon energy for Li^+ (for $L = 0$, and $L = 2$, respectively). They are similar in shape to the He two-photon partial cross sections with their $1snp\,^1P_1$ peak structures (and so also differ from the one-photon case). As with He, the Li^+ two-photon partial cross sections are orders of magnitude lower than the one-photon case, and also like He, the non-resonant Li^+ $L = 0$ partial cross section is about an order of magnitude lower than that of $L = 2$. And as with the one-photon Li^+ to He comparison, the two-photon Li^+ partial cross sections are lower than the He, about an order of magnitude.

From Tables 3.7, 3.8 it is seen that there is a discrepancy of ~ 0.3 eV between established and computed ionization values, and a discrepancy of $\sim 0.5 - 0.6$ eV between established and computed peak values − close to the ground state discrepancy of ~ 0.6 eV listed in Table 2.8.

When the calculated $L = 0$ and $L = 2$ plots are summed (total cross section), the resultant cross section matches well to that of Emmanouilidou *et al*'s work [44], which models two-photon ionization of Li^+ employing single-channel quantum defect theory: when the shift is accounted for, the peaks occur close to theirs (62.2 eV $1s2p(^1P_1)$, 69.7 eV $1s3p(^1P_1)$, 72.3 eV $1s4p(^1P_1)$ and 73.5 eV $1s5p(^1P_1)$); and the (L-partial sum) cross section baseline between $50 - 55$ eV is within the same order of magnitude as theirs (both between $10^{-53} - 10^{-52}$ cm^4 s), however the shape is slightly different here, being slightly convex (-downward) in

[1] There is one exception to the agreement, from the 20.73 eV (21.23 nm) data point, which occurs on-resonance in Figure 3.6. Even a shift of 0.01 eV changes (lowers) the value 5 orders of magnitude.

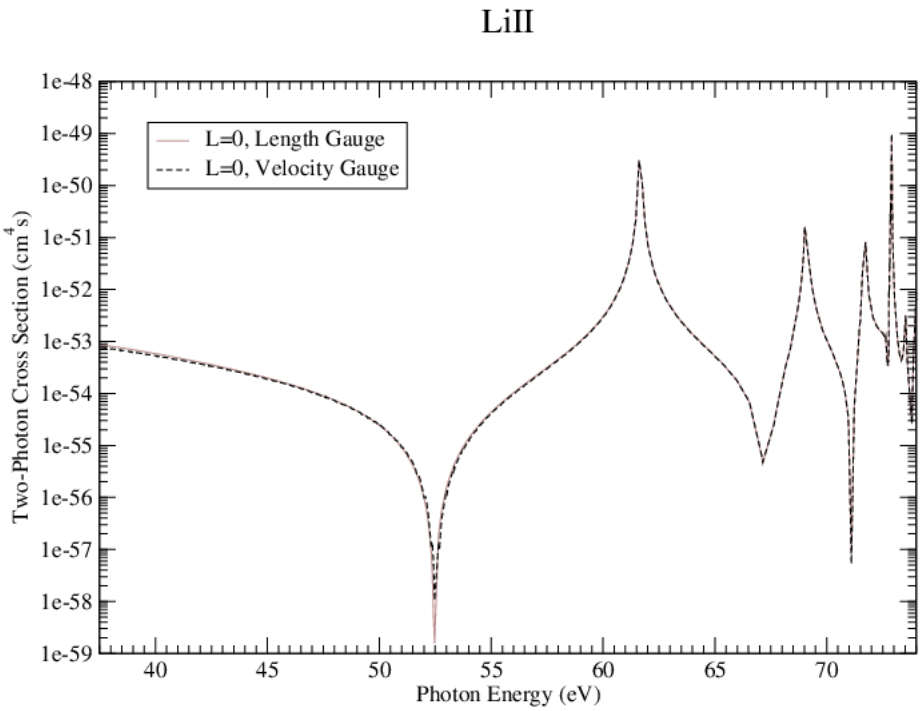

Figure 3.7: Two-photon, $L = 0$ ionization of Li^+ in the 37.5-74 eV region, with $n_b = 110$ B-splines of order $k_b = 9$, 17 box-sizes R varied between $50 - 58$ $a.u.$, and 1100 included orbital configurations.

Table 3.7: Energy features of $Li^+ \rightarrow Li^{2+}$ two-photon, $L = 0$ cross section plot, compared to the currently accepted ionization energy and various energy levels.

	Calculated eV		NIST eV	Discrepancy eV	Discrepancy %
		Ionization	75.6401		
1st Point	37.5457	$\hookrightarrow \div 2$	37.8201	0.2744	0.7255
1st Peak	61.6124	$1s2p(^1P_1)$	62.2163	0.6039	0.9706
2nd Peak	69.0192	$1s3p(^1P_1)$	69.6485	0.6293	0.9035
3rd Peak	71.7323	$1s4p(^1P_1)$	72.2617	0.5294	0.7326
4th Peak	72.9035	$1s5p(^1P_1)$	73.4774	0.5739	0.7811

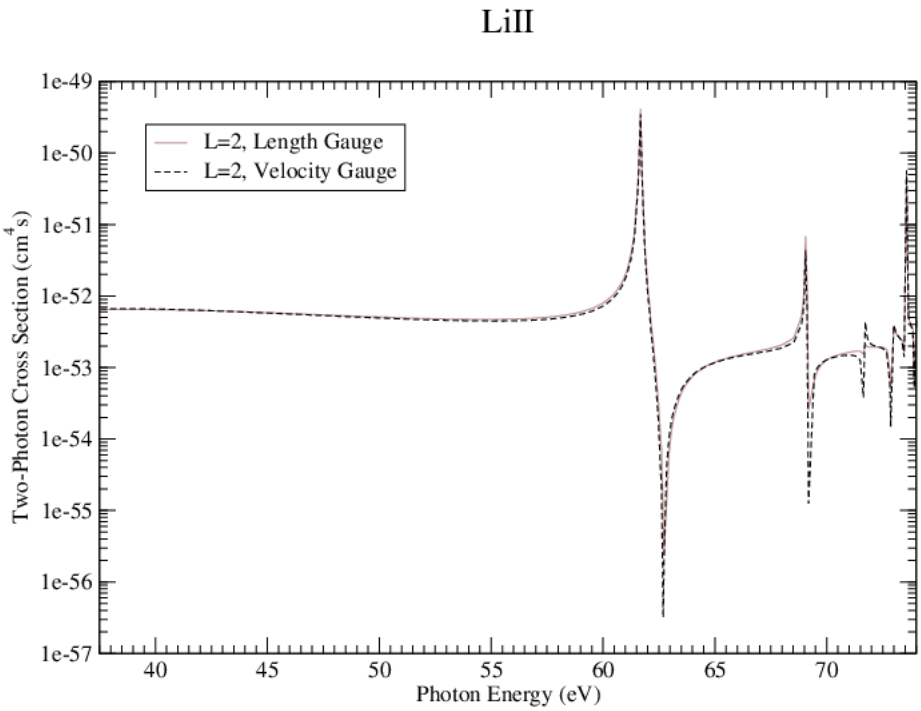

Figure 3.8: Two-photon, $L = 2$ ionization of Li^+ in the 37.5-74 eV region, with $n_b = 110$ B-splines of order $k_b = 9$, 17 box-sizes R varied between $50 - 58$ $a.u.$, and 1100 included orbital configurations.

Table 3.8: Energy features of $Li^+ \rightarrow Li^{2+}$ two-photon, $L = 2$ cross section plot, compared to the currently accepted ionization energy and various energy levels.

	Calculated eV		NIST eV	Discrepancy eV	Discrepancy %
		Ionization	75.6401		
1st Point	37.5385	$\hookrightarrow \div 2$	37.8201	0.2816	0.7446
1st Peak	61.6828	$1s2p(^1P_1)$	62.2163	0.5335	0.8575
2nd Peak	69.0504	$1s3p(^1P_1)$	69.6485	0.5981	0.8587
3rd Peak	71.7216	$1s4p(^1P_1)$	72.2617	0.5401	0.7474
4th Peak	72.9913	$1s5p(^1P_1)$	73.4774	0.4861	0.6616

this region (for the sum of Figures 3.7 and 3.8).

Note: two-photon auto-ionizing state peaks from ${}^1S$, ${}^1D$ terms would occur at higher energies, beyond about 75 eV (the lowest post-ionization energy levels are about 150 eV, and half that value (two photons) is about 75 eV).

3.2.3 Two-Photon Cross Section of Ne^{8+}

Figures 3.9 and 3.10 display plots of two-photon partial-ionization cross sections vs photon energy for Ne^{8+} (for $L = 0$, and $L = 2$, respectively). As with He and Li^+, the Ne^{8+} two-photon partial cross sections differ from the one-photon case, and the Ne^{8+} two-photon partial cross sections are similar to that of He and Li^+, with $1snp\,{}^1P_1$ peak structures, but there is a notable difference: Ne^{8+} has additional peaks due to interference from two-photon (two-electron excitation) auto-ionizing states, which have relatively (compared to He and Li^+) low enough energy to appear on the plot. These additional peaks represent $npn'p$, $n, n' = 2, ...$ states and such peaks occur at different places on the $L = 0$ and $L = 2$ plots, as the states are on different total angular momentum channels (${}^1S_0$ and ${}^1D_2$, respectively).

As with He and Li^+, the two-photon partial cross sections of Ne^{8+} are orders of magnitude lower than the one-photon case, and also like He and Li^+, the non-resonant Ne^{8+} $L = 0$ partial cross section is about an order of magnitude lower than that of $L = 2$. And as with the one-photon comparison with He and Li^+, the two-photon Ne^{8+} partial cross sections are lower than that of He and Li^+, being about three orders of magnitude less than Li^+.

From Tables 3.9, 3.10 it is seen that there is a discrepancy of ~ 1 eV between established and computed ionization values, and a discrepancy of $\sim$ 1-2 [1] eV between established and computed peak values − these discrepancies are lower than the ground state discrepancy of ~ 3.5 eV. Like with single-photon Ne^{8+} and Ar^{16+}, these differences in expected discrepancies could be due to the non-negligible higher state discrepancies, an increase of relativistic

[1] Except one of the entries marked with an asterisk − these entries are peaks due to the strong coupling between the $2s^2({}^1S_0)$ and $2p^2({}^1S_0)$ configurations (this was established by running tests excluding $2s^2$, $2p^2$, or both from the configuration files to see how their presence affected the peaks). Peaks 3 and 4 also exhibit similar interference, being formed from $2s3s({}^1S_0)$ and $2p3p({}^1S_0)$ coupling.

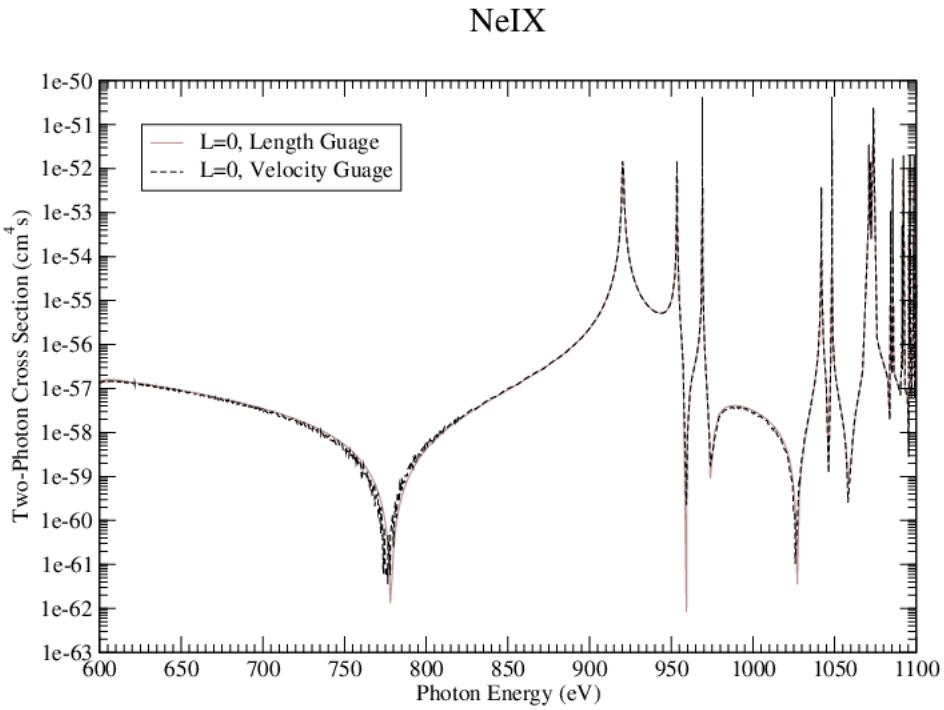

Figure 3.9: Two-photon, $L = 0$ ionization of Ne^{8+} in the 600-1100 eV region, with $n_b = 170$ B-splines of order $k_b = 9$, 17 box-sizes R varied between $20 - 28$ $a.u.$, and 1600 included orbital configurations.

Table 3.9: Energy features of $Ne^{8+} \rightarrow Ne^{9+}$ two-photon, $L = 0$ cross section plot, compared to the currently accepted ionization energy and various energy levels.

	Calculated eV		NIST eV	Discrepancy eV	Discrepancy %
		Ionization	1195.808		
1st Point	596.997	$\hookrightarrow \div 2$	597.904	0.907	0.1517
1st Peak	920.123	$1s2p(^1P_1)$	922.016	1.893	0.2053
		$2p^2(^1S_0)$	1940.623		
2nd Peak	953.501	$\hookrightarrow \div 2$	970.312	16.811*	1.733
		$2p^2(^1S_0)$	1940.623		
3rd Peak	969.065	$\hookrightarrow \div 2$	970.312	1.247*	0.1285
		$2p3p(^1S_0)$	[no data]		
4th Peak	1041.87	$\hookrightarrow \div 2$	[N/A]	[N/A]	[N/A]
		$2p3p(^1S_0)$	[no data]		
5th Peak	1048.34	$\hookrightarrow \div 2$	[N/A]	[N/A]	[N/A]
6th Peak	~ 1072	$1s3p(^1P_1)$	1073.77	~ 2	~ 0.2

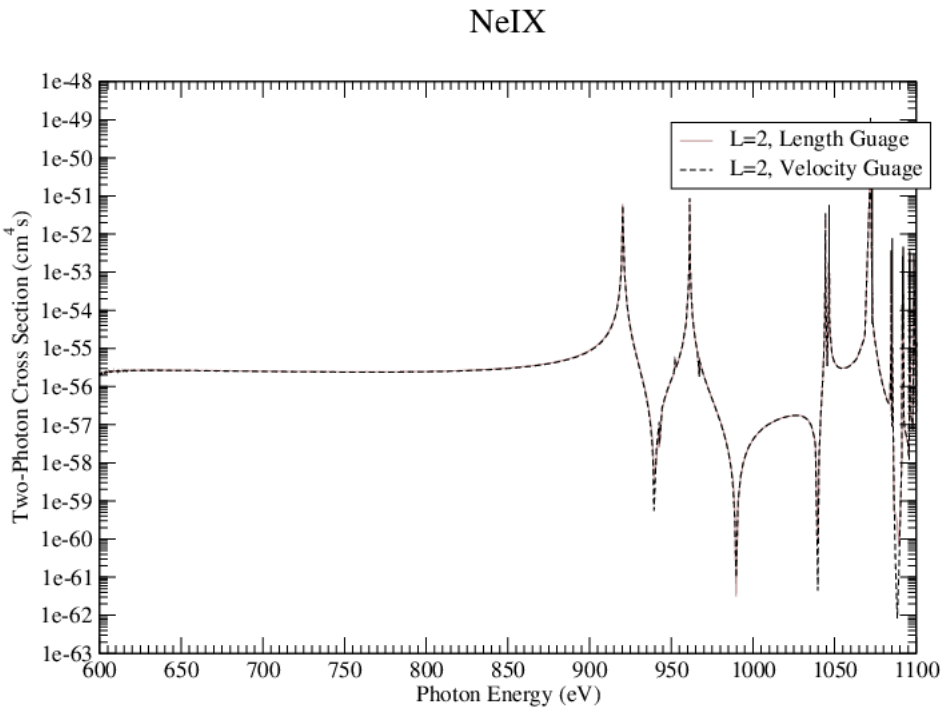

Figure 3.10: Two-photon, $L = 2$ ionization of Ne^{8+} in the 600-1100 eV region, with $n_b = 170$ B-splines of order $k_b = 9$, 17 box-sizes R varied between $20 - 28$ $a.u.$, and 1600 included orbital configurations.

Table 3.10: Energy features of $Ne^{8+} \rightarrow Ne^{9+}$ two-photon, $L = 2$ cross section plot, compared to the currently accepted ionization energy and various energy levels.

	Calculated eV		NIST eV	Discrepancy eV	Discrepancy %
		Ionization	1195.808		
1^{st} Point	597.110	$\hookrightarrow \div 2$	597.904	0.794	0.1328
1^{st} Peak	920.272	$1s2p(^1P_1)$	922.016	1.744	0.1892
		$2p^2(^1D_2)$	1925.537		
2^{nd} Peak	961.306	$\hookrightarrow \div 2$	962.769	1.463	0.1520
		$2p3p(^1D_2)$	[no data]		
3^{rd} Peak	1044.34	$\hookrightarrow \div 2$	[N/A]	[N/A]	[N/A]
		$2p3p(^1D_2)$	[no data]		
4^{th} Peak	1046.61	$\hookrightarrow \div 2$	[N/A]	[N/A]	[N/A]
5^{th} Peak	1071.94	$1s3p(^1P_1)$	1073.77	1.83	0.1704

effects, the less justified use of the dipole approximation, or the increased propagation of the one-electron state error with higher Z.

The calculated cross section plot is in agreement with the second-order perturbation theory modelling of Novikov and Hopersky [45]: their $1s2p(^1P_1)$ and $1s3p(^1P_1)$ one-photon resonance peaks (these are their only peaks) are comparable, occurring at around 920 eV and 1070 eV, respectively; and their cross section baseline at $600 - 800$ eV is close to the calculations of this study, both within the same order of magnitude (both between $10^{-56} - 10^{-55}$ cm^{-4} s). A data point for the photo-ionization cross section of Ne^{8+} was reported using the Linac Coherent Light Source XFEL for an experiment by Doumy *et al* [46]: it measured a cross section of 7×10^{-54} cm^{4}s at 1110 eV − the (L-partial sum) value (of Figures 3.9, 3.10) at this photon energy is 3×10^{-54} cm^{4}s, which is within the same order of magnitude (the agreement could potentially be improved (or worsened) by accounting for the shift, since there are nearby resonances. Also note this is in a less reliable region of Figures 3.9, 3.10). Sytcheva *et al*'s time-dependent CI singles model [47], when convoluted with a spectral distribution function, was able to simulate Doumy's off-resonance data point much better than Novikov and Hopersky, by increasing the $1s3p(^1P_1)$ (and $1s2p(^1P_1)$) peak width − note the data of this study lacks this feature which could potentially produce better agreement. The cross section values are in agreement with the Green-function calculations in Ref. [48].

3.2.4 Two-Photon Cross Section of Ar^{16+}

Figures 3.11, and 3.12 display plots of two-photon partial-ionization cross sections vs photon energy for Ar^{16+} (for $L = 0$, and $L = 2$, respectively). As with the other species, the two-photon partial cross sections differ from the one-photon case, and the two-photon partial cross sections of Ar^{16+} are quite similar to Ne^{8+}, having the $1snp\,^1P_1$ peak structures as well as the $npn'p$, $n, n' = 2, ...$ interference peaks, with the latter peaks also occurring in different places on the $L = 0$ and $L = 2$ plots.

As with the other species, the two-photon partial cross sections of Ar^{16+} are orders of magnitude lower than the one-photon case, and the non-resonant $L = 0$ partial cross section

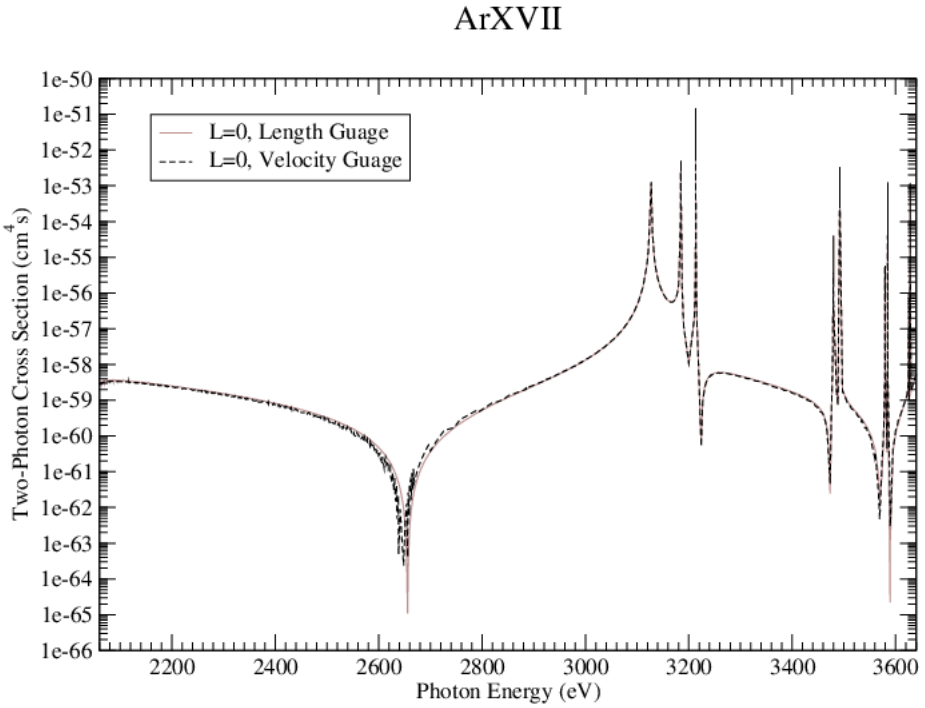

Figure 3.11: Two-photon, $L = 0$ ionization of Ar^{16+} in the 2060-3640 eV region, with $n_b = 170$ B-splines of order $k_b = 9$, 17 box-sizes R varied between $10 - 14.8$ $a.u.$, and 1600 included orbital configurations.

Table 3.11: Energy features of $Ar^{16+} \rightarrow Ar^{17+}$ two-photon, $L = 0$ cross section plot, compared to the currently accepted ionization energy and various energy levels.

	Calculated eV		NIST eV	Discrepancy eV	Discrepancy %
		Ionization	4120.67		
1st Point	2052.84	$\hookrightarrow \div 2$	2060.34	7.70	0.3737
1st Peak	3127.23	$1s2p(^1P_1)$	3286.42	159.19	4.844
		$2p^2(^1S_0)$	6453.33		
2nd Peak	3184.62	$\hookrightarrow \div 2$	3226.67	42.05*	1.303
		$2p^2(^1S_0)$	6453.33		
3rd Peak	3213.40	$\hookrightarrow \div 2$	3226.67	13.27*	0.4113
		$2p3p(^1S_0)$	[no data]		
4th Peak	3479.71	$\hookrightarrow \div 2$	[N/A]	[N/A]	[N/A]
		$2p3p(^1S_0)$	[no data]		
5th Peak	3492.12	$\hookrightarrow \div 2$	[N/A]	[N/A]	[N/A]
6th Peak	3584.80	$1s3p(^1P_1)$	3683.85	99.05	2.689

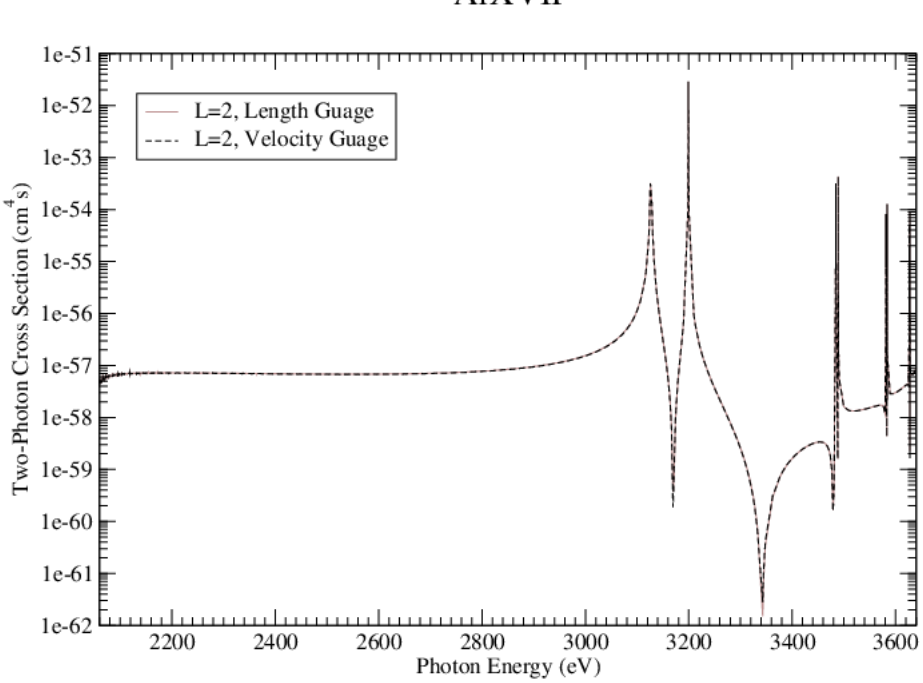

Figure 3.12: Two-photon, $L = 2$ ionization of Ar^{16+} in the 2060-3640 eV region, with $n_b = 170$ B-splines of order $k_b = 9$, 17 box-sizes R varied between $10 - 14.8$ $a.u.$, and 1600 included orbital configurations.

Table 3.12: Energy features of $Ar^{16+} \rightarrow Ar^{17+}$ two-photon, $L = 2$ cross section plot, compared to the currently accepted ionization energy and various energy levels.

	Calculated eV		NIST eV	Discrepancy eV	Discrepancy %
		Ionization	4120.67		
1^{st} Point	2052.95	$\hookrightarrow \div 2$	2060.34	7.39	0.3587
1^{st} Peak	3125.48	$1s2p(^1P_1)$	3286.42	160.94	4.897
		$2p^2(^1D_2)$	6426.52		
2^{nd} Peak	3199.18	$\hookrightarrow \div 2$	3213.26	14.08	0.4382
		$2p3p(^1D_2)$	[no data]		
3^{rd} Peak	3484.32	$\hookrightarrow \div 2$	[N/A]	[N/A]	[N/A]
		$2p3p(^1D_2)$	[no data]		
4^{th} Peak	3488.91	$\hookrightarrow \div 2$	[N/A]	[N/A]	[N/A]
5^{th} Peak	3581.42	$1s3p(^1P_1)$	3683.85	102.43	2.781

is about an order of magnitude lower than $L = 2$. And as with the one-photon comparison with the other species, Ar^{16+} has the lowest two-photon partial cross sections, being about two orders of magnitude less than Ne^{8+}.

From Tables 3.11, 3.12 it is seen that there is a discrepancy of ~ 7 eV between established and computed ionization values, and a discrepancy of $\sim 3 - 160$ eV between established and computed peak values − these discrepancies vary over quite a range compared to the ground state discrepancy of ~ 33 eV. This could be due to a greater impact by the relativistic effects, or the less justified use of the dipole approximation or the increased propagation of the one-electron state error for the much higher atomic number of Ar^{16+}.

As with Ne^{8+}, the 2^{nd} and 3^{rd}, and 4^{th} and 5^{th} peaks are due to $2s^2(^1S_0)$ and $2p^2(^1S_0)$, and $2s3s(^1S_0)$ and $2p3p(^1S_0)$ coupling. The cross section values are also in agreement with the Green-function calculations in Ref. [48].

There are no known Ar^{16+} two-photon ionization cross section experiments to date.

3.3 Three-Photon Cross Section

Figures 3.13, 3.14, 3.15, 3.16, 3.17, 3.18, 3.19, 3.20 show the calculated three photon partial-ionization cross sections ($L = 1$, $L = 3$) of He, Li^+, Ne^{8+} and Ar^{16+} (respectively) from the ground state $1s^2(^1S_0)$ to $^1P_0$, $^1F_3$ states above the first ionization threshold. Total three-photon ionization cross sections are obtained by the addition of all the L-partial cross sections of equation (2.7), but note these are logarithmic plots. The final state in this case will be dominated by bound states and the free $1s\varepsilon p(^1P_1)$ or $1s\varepsilon f(^1F_3)$ continua. The results of both length and velocity gauge are plotted. The three-photon cross sections are composed of strong peak structures, which appear in both $L = 1$ and $L = 3$ symmetries, due to two-photon resonance with the intermediate states $1snd\,^1D_2$, $n = 3, 4, ...$, and also in the $L = 1$ symmetry there are additional peaks due to two-photon resonance states of the type $1sns\,^1S_0$, $n = 2, 3, ...$. The $^1P_1$ ($L = 1$) final state is obtained by the coherent superposition of the following two absorption channels, which can both reach a final angular momentum of $L = 1$: $S \to P \to S \to P$ and $S \to P \to D \to P$. For $^1F_3$ ($L = 3$), the only path is: $S \to P \to D \to F$.

Tables 3.13, 3.14, 3.15, 3.16, 3.17, 3.18, 3.19, 3.20 list the energy positions of various features in the cross sections, and their comparisons with current NIST values. The first data point in each represents a third of the ionization energy (of $He \to He^+$, $Li^+ \to Li^{2+}$, $Ne^{8+} \to Ne^{9+}$ and $Ar^{16+} \to Ar^{17+}$) (the established ionization energy is divided by three (three photons) to compare). The other entries are the positions of the highest points of peaks, which are compared with various resonances, closely matching in value to currently established energy states. Each cross section was calculated up to half the ionization energy of the respective species (any more than this and two-photon ionization would dominate).

3.3.1 Three-Photon Cross Section of He

Figures 3.13 and 3.14 display plots of three-photon partial-ionization cross sections vs photon energy for He (for $L = 1$, and $L = 3$, respectively). The shape of the cross sections are similar to the two-photon $L = 0$ and $L = 2$ cases, in that they have strong peak structures, but this time they are due to two-photon intermediate resonances of the type $1snd\,^1D_2,\ \ n = 3, 4, ...$, and in the $L = 1$ partial cross section there are also two-photon resonances from $1sns\,^1S_0,\ \ n = 2, 3, ...$ states. As with the one-photon to two-photon cross section comparison, the cross section values of this three-photon case are even lower, being many orders of magnitude lower than the two-photon case (expected, as three photon cross section is a product of three small areas and two small time durations). It's harder to compare the non-resonant regions of the $L = 1$ and $L = 3$ partial sections than it is to compare the two-photon $L = 0$ and $L = 2$ partial cross sections, because the $L = 1$ cross section varies more than the $L = 0$ does (sometimes the $L = 1$ cross section dominates and sometimes $L = 3$ does).

From Tables 3.13, 3.14 it is seen that there is a discrepancy of ~ 0.2 eV between established and computed ionization values, and a discrepancy of $\sim 0.2 - 0.3$ eV between established and computed peak values − less than the ground state discrepancy of ~ 0.5 eV listed in Table 2.8.

Three-photon ionization may have been observed in a study [49], but it could not be confirmed as it couldn't be separated from the background signal of the third harmonic of single-photon ionization in that experiment, which was of the same order of magnitude.

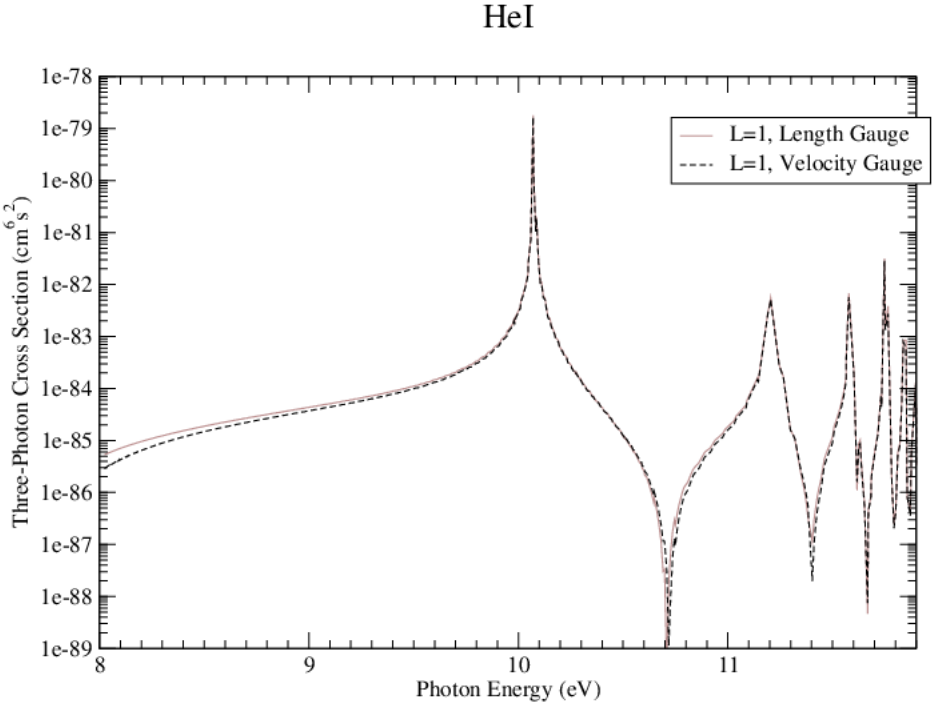

Figure 3.13: Three-photon, $L = 1$ ionization of He in the 8-11.9 eV region, with $n_b = 600$ B-splines of order $k_b = 9$, 17 box-sizes R varied between $140 - 160$ $a.u.$, and 1300 included orbital configurations.

Table 3.13: Energy features of He $\rightarrow$ He^+ three-photon, $L = 1$ cross section plot.

	Calculated eV		NIST eV	Discrepancy eV	Discrepancy %
		Ionization	24.58739		
1st Point	8.02419	$\hookrightarrow \div 3$	8.19580	0.17161	2.094
		$1s2s(^1S_0)$	20.6158		
1st Peak	10.0704	$\hookrightarrow \div 2$	10.3079	0.2375	2.304
		$1s3s(^1S_0)$	22.9203		
2nd Peak	11.2047	$\hookrightarrow \div 2$	11.4602	0.2555	2.229
		$1s3d(^1D_2)$	23.0741		
2nd Peak	11.2047	$\hookrightarrow \div 2$	11.5371	0.3324	2.881
		$1s4s(^1S_0)$	23.6736		
3rd Peak	11.5778	$\hookrightarrow \div 2$	11.8368	0.2590	2.188
		$1s4d(^1D_2)$	23.7363		
Sub 3rd Peak	11.6319	$\hookrightarrow \div 2$	11.8682	0.2363	1.991
		$1s5s(^1S_0)$	24.0112		
4th Peak	11.7479	$\hookrightarrow \div 2$	12.0056	0.2577	2.146
		$1s5d(^1D_2)$	24.0428		
Sub 4th Peak	11.7650	$\hookrightarrow \div 2$	12.0214	0.2564	2.133
		$1s6s(^1S_0)$	24.1912		
5th Peak	11.8507	$\hookrightarrow \div 2$	12.0956	0.2449	2.025
		$1s6d(^1D_2)$	24.2092		
5th Peak	11.8507	$\hookrightarrow \div 2$	12.1046	0.2539	2.098

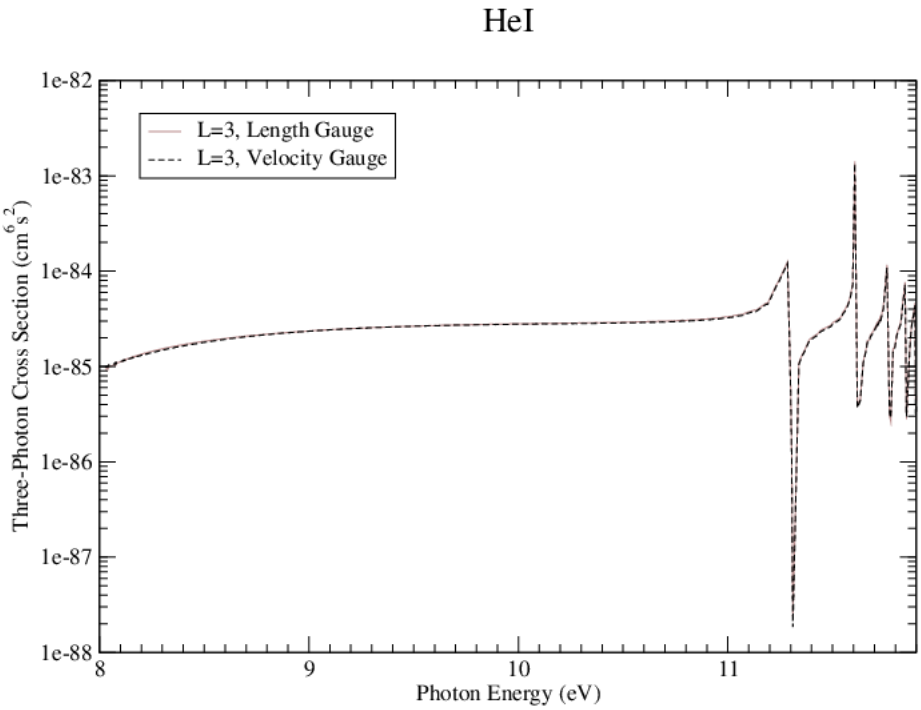

Figure 3.14: Three-photon, $L = 3$ ionization of He in the 8-11.9 eV region, with $n_b = 600$ B-splines of order $k_b = 9$, 17 box-sizes R varied between $140 - 160$ $a.u.$, and 1300 included orbital configurations.

Table 3.14: Energy features of He $\rightarrow$ He$^+$ three-photon, $L = 3$ cross section plot.

	Calculated eV		NIST eV	Discrepancy eV	Discrepancy %
		Ionization	24.58739		
1$^{\text{st}}$ Point	8.02700	$\hookrightarrow \div 3$	8.19580	0.16880	2.060
		$1s3d(^1D_2)$	23.0741		
1$^{\text{st}}$ Peak	11.2853	$\hookrightarrow \div 2$	11.5371	0.2518	2.183
		$1s4d(^1D_2)$	23.7363		
2$^{\text{nd}}$ Peak	11.6062	$\hookrightarrow \div 2$	11.8682	0.2620	2.208
		$1s5d(^1D_2)$	24.0428		
3$^{\text{rd}}$ Peak	11.7601	$\hookrightarrow \div 2$	12.0214	0.2613	2.174
		$1s6d(^1D_2)$	24.2092		
4$^{\text{th}}$ Peak	11.8465	$\hookrightarrow \div 2$	12.1046	0.2581	2.132

3.3.2 Three-Photon Cross Section of Li^+

Figures 3.15 and 3.16 display plots of three-photon partial-ionization cross sections vs photon energy for Li^+ (for $L = 1$, and $L = 3$, respectively). The shape of the cross sections are similar to the He three-photon partial cross sections, with corresponding peaks/resonances, although appearing as sub-peaks in places (due to mixing of states or lack of resolution). As with three-photon He, and the two-photon vs one-photon comparisons, the three-photon Li^+ cross sections are many orders of magnitude lower than the two-photon cross sections. As with He, the non-resonant cross sections of $L = 1$ and $L = 3$ are comparable.

From Tables 3.15, 3.16 it is seen that there is a discrepancy of $\sim 0.1 - 0.2$ eV between established and computed ionization values, and a discrepancy of $\sim 0.2 - 0.4$ eV between established and computed peak values − less than the ground state discrepancy of ~ 0.6 eV listed in Table 2.8.

Note: the sub peak on the right of the 2^{nd} peak of the $L = 0$ plot is formed by a mix of $1s3d(^1S_0)$ and $1s3d(^1D_2)$, even though it's listed in Table 3.15 as $1s3d(^1D_2)$.

There are no known Li^+ three-photon ionization cross section experiments to date.

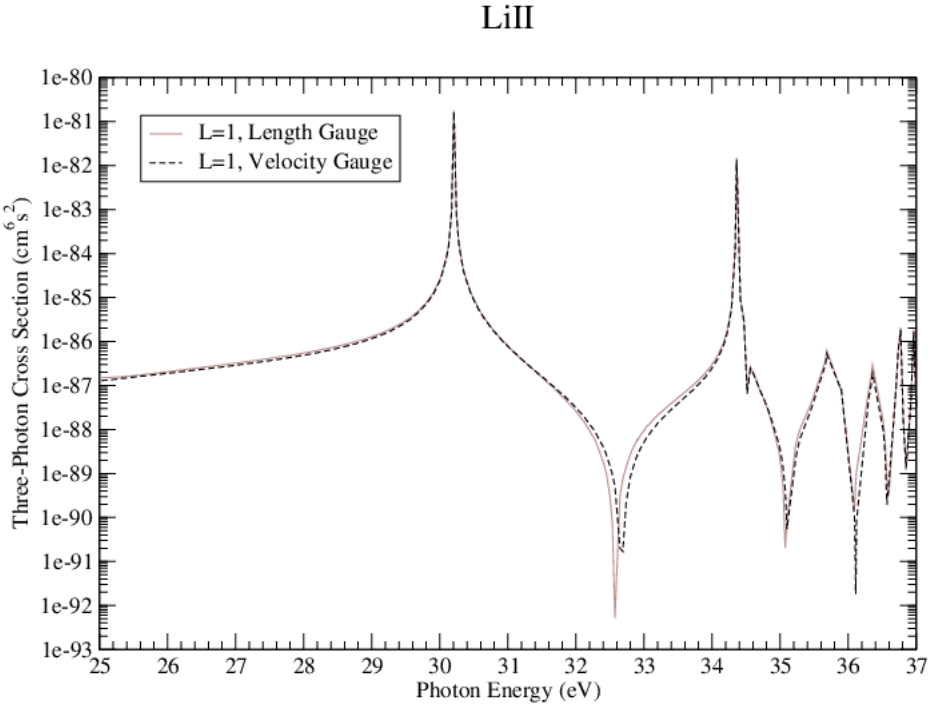

Figure 3.15: Three-photon, $L = 1$ ionization of Li^+ in the 25-37 eV region, with $n_b = 110$ B-splines of order $k_b = 9$, 17 box-sizes R varied between $50 - 58$ $a.u.$, and 1100 included orbital configurations.

Table 3.15: Energy features of $Li^+ \rightarrow Li^{2+}$ three-photon, $L = 1$ cross section plot.

	Calculated eV		NIST eV	Discrepancy eV	Discrepancy %
		Ionization	75.6401		
1st Point	25.0291	$\hookrightarrow \div 3$	25.2134	0.1843	0.7310
		$1s2s(^1S_0)$	60.9227		
1st Peak	30.2062	$\hookrightarrow \div 2$	30.4614	0.2552	0.8378
		$1s3s(^1S_0)$	69.2796		
2nd Peak	34.3610	$\hookrightarrow \div 2$	34.6398	0.2788	0.8049
		$1s3d(^1D_2)$	69.5891		
Sub 2nd Peak	34.5612	$\hookrightarrow \div 2$	34.7946	0.2334	0.6708
		$1s4s(^1S_0)$	72.1088		
3rd Peak	35.6845	$\hookrightarrow \div 2$	36.0544	0.3699	1.026
		$1s4d(^1D_2)$	72.2370		
3rd Peak	35.6845	$\hookrightarrow \div 2$	36.1185	0.4340	1.202
		$1s5s(^1S_0)$	73.3973		
4th Peak	36.3581	$\hookrightarrow \div 2$	36.6987	0.3406	0.9281
		$1s5d(^1D_2)$	73.4624		
4th Peak	36.3581	$\hookrightarrow \div 2$	36.7312	0.3731	1.016
		$1s6s(^1S_0)$	74.0905		
5th Peak	36.7705	$\hookrightarrow \div 2$	37.0453	0.2748	0.7418
		$1s6d(^1D_2)$	74.1280		
5th Peak	36.7705	$\hookrightarrow \div 2$	37.0640	0.2935	0.7919

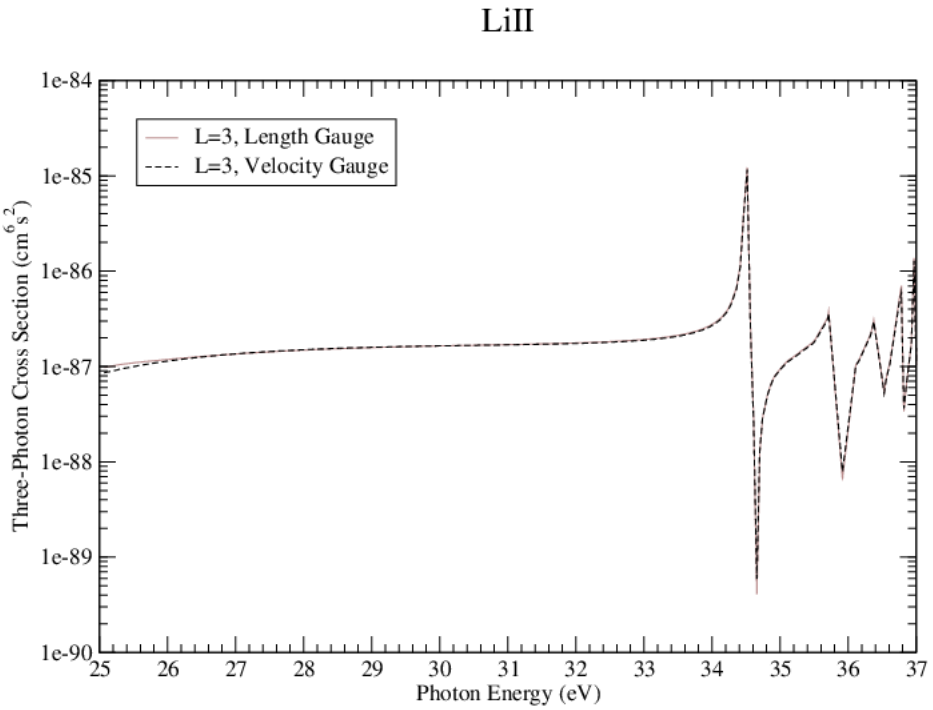

Figure 3.16: Three-photon, $L = 3$ ionization of Li^+ in the 25-37 eV region, with $n_b = 110$ B-splines of order $k_b = 9$, 17 box-sizes R varied between $50 - 58$ $a.u.$, and 1100 included orbital configurations.

Table 3.16: Energy features of $Li^+ \rightarrow Li^{2+}$ three-photon, $L = 3$ cross section plot.

	Calculated eV		NIST eV	Discrepancy eV	Discrepancy %
		Ionization	75.6401		
1st Point	25.0705	$\hookrightarrow \div 3$	25.2134	0.1429	0.5668
		$1s3d(^1D_2)$	69.5891		
1st Peak	34.5163	$\hookrightarrow \div 2$	34.7946	0.2783	0.7998
		$1s4d(^1D_2)$	72.2370		
2nd Peak	35.7122	$\hookrightarrow \div 2$	36.1185	0.4063	1.125
		$1s5d(^1D_2)$	73.4624		
3rd Peak	36.3747	$\hookrightarrow \div 2$	36.7312	0.3565	0.9706
		$1s6d(^1D_2)$	74.1280		
4th Peak	36.7799	$\hookrightarrow \div 2$	37.0640	0.2841	0.7665

3.3.3 Three-Photon Cross Section of Ne^{8+}

Figures 3.17 and 3.18 display plots of three-photon partial-ionization cross sections vs photon energy for Ne^{8+} (for $L = 1$, and $L = 3$, respectively). The shape of the cross sections are similar to the He and Li^+ three-photon partial cross sections, although poor quality is evident towards the end, after the 3^{rd} peak in both partial cross sections. A large deviation is noticeable between the length and velocity gauges in the $L = 1$ cross section. As with three-photon He and Li^+, and the two-photon vs one-photon comparisons, the three-photon Ne^{8+} cross sections are many orders of magnitude lower than the two-photon cross sections. As with He and Li^+, the non-resonant cross sections of $L = 1$ and $L = 3$ are comparable.

From Tables 3.17, 3.18 it is seen that there is a discrepancy of $\sim 0.5 - 0.6$ eV between established and computed ionization values, and a discrepancy of $\sim 0.8 - 1.0$ [1] eV between established and computed peak values − less than the ground state discrepancy of ~ 3.5 eV listed in Table 2.9.

The poor quality towards the end of the plots is a numerical problem due to low resolution. Tests were done with additional states added in to improve this, but these formed problems in other areas and more tweaking would be needed to optimize successfully.

There are no known Ne^{8+} three-photon ionization cross section experiments to date.

[1] Except one of the entries marked with an asterisk, which is off-put due to interference: this peak is not solely due to the $1s3d(^1D_2)$ configuration, but also formed and dominated by $1s3s(^1S_0)$.

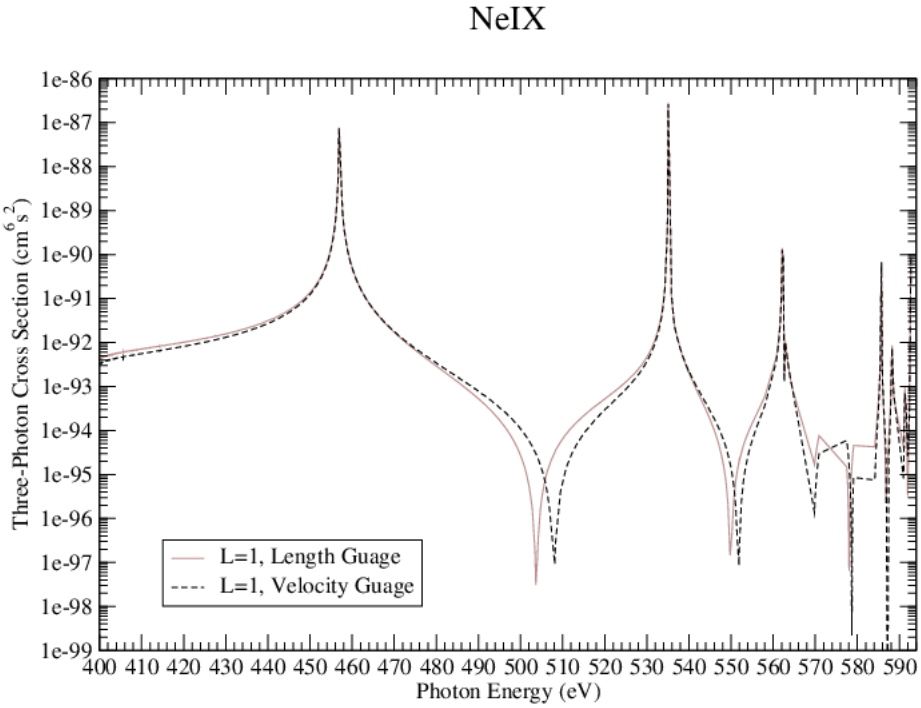

Figure 3.17: Three-photon, $L = 1$ ionization of Ne^{8+} in the 400-594 eV region, with $n_b = 170$ B-splines of order $k_b = 9$, 17 box-sizes R varied between $20 - 28$ $a.u.$, and 1600 included orbital configurations.

Table 3.17: Energy features of $Ne^{8+} \rightarrow Ne^{9+}$ three-photon, $L = 1$ cross section plot.

	Calculated eV		NIST eV	Discrepancy eV	Discrepancy %
		Ionization	1195.808		
1st Point	398.058	$\hookrightarrow \div 3$	398.603	0.545	0.1367
		$1s2s(^1S_0)$	915.336		
1st Peak	456.905	$\hookrightarrow \div 2$	457.668	0.763	0.1667
		$1s3s(^1S_0)$	1071.829		
2nd Peak	535.077	$\hookrightarrow \div 2$	535.915	0.838	0.1564
		$1s3d(^1D_2)$	1074.001		
2nd Peak	535.077	$\hookrightarrow \div 2$	537.001	1.924*	0.3583
		$1s4s(^1S_0)$	1126.280		
3rd Peak	562.164	$\hookrightarrow \div 2$	563.140	0.976	0.1733
		$1s4d(^1D_2)$	[no data]		
Sub 3rd Peak	562.884	$\hookrightarrow \div 2$	[N/A]	[N/A]	[N/A]

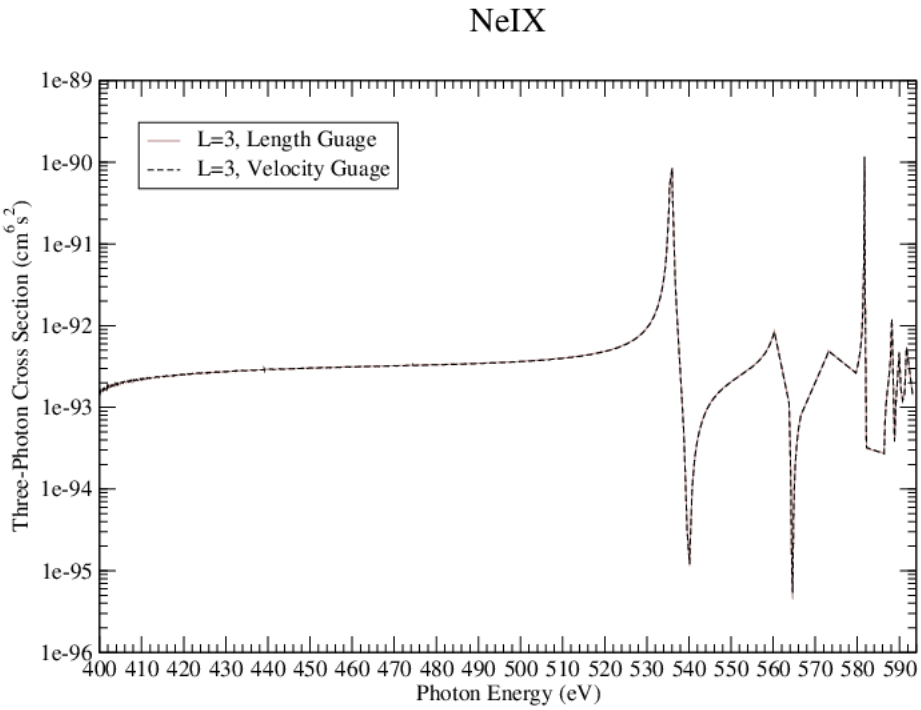

Figure 3.18: Three-photon, $L = 3$ ionization of Ne^{8+} in the 400-594 eV region, with $n_b = 170$ B-splines of order $k_b = 9$, 17 box-sizes R varied between $20 - 28$ $a.u.$, and 1600 included orbital configurations.

Table 3.18: Energy features of $Ne^{8+} \rightarrow Ne^{9+}$ three-photon, $L = 3$ cross section plot.

	Calculated eV		NIST eV	Discrepancy eV	Discrepancy %
		Ionization	1195.808		
1^{st} Point	398.033	$\hookrightarrow \div 3$	398.603	0.570	0.1430
		$1s3d(^1D_2)$	1074.001		
1^{st} Peak	536.011	$\hookrightarrow \div 2$	537.001	0.990	0.1844
		$1s4d(^1D_2)$	[no data]		
2^{nd} Peak	560.282	$\hookrightarrow \div 2$	[N/A]	[N/A]	[N/A]
		$1s5d(^1D_2)$	[no data]		
3^{rd} Peak	573.085	$\hookrightarrow \div 2$	[N/A]	[N/A]	[N/A]
		$1s6d(^1D_2)$	[no data]		
4^{th} Peak	581.716	$\hookrightarrow \div 2$	[N/A]	[N/A]	[N/A]

3.3.4 Three-Photon Cross Section of Ar^{16+}

Figures 3.19 and 3.20 display plots of three-photon partial-ionization cross sections vs photon energy for Ar^{16+} (for $L = 1$, and $L = 3$, respectively). The shape of the cross sections are similar to the three-photon partial cross sections of the other species, and as with Ne^{8+}, there is a noticeable large deviation between the length and velocity gauges in the $L = 1$ cross section. As with the other species, the three-photon Ar^{16+} cross sections are many orders of magnitude lower than the two-photon case, and the non-resonant cross sections of $L = 1$ and $L = 3$ are comparable.

From Tables 3.19, 3.20 it is seen that there is a discrepancy of ~ 0.5 eV between established and computed ionization values, and a discrepancy of $\sim 0.5 - 9.0$ eV between established and computed peak values − less than the ground state discrepancy of ~ 33 eV listed in Table 2.10.

As with Ne^{8+}, the peaks (except the 1^{st}) in the $L = 1$ plot are constituted by a mix of ^1S and ^1D states. The $L = 3$ plot is only constituted by ^1D states, and when comparing the two plots it is seen that $L = 3$ plot's peaks are shifted a bit to the right.

There are no known Ar^{16+} three-photon ionization cross section experiments to date.

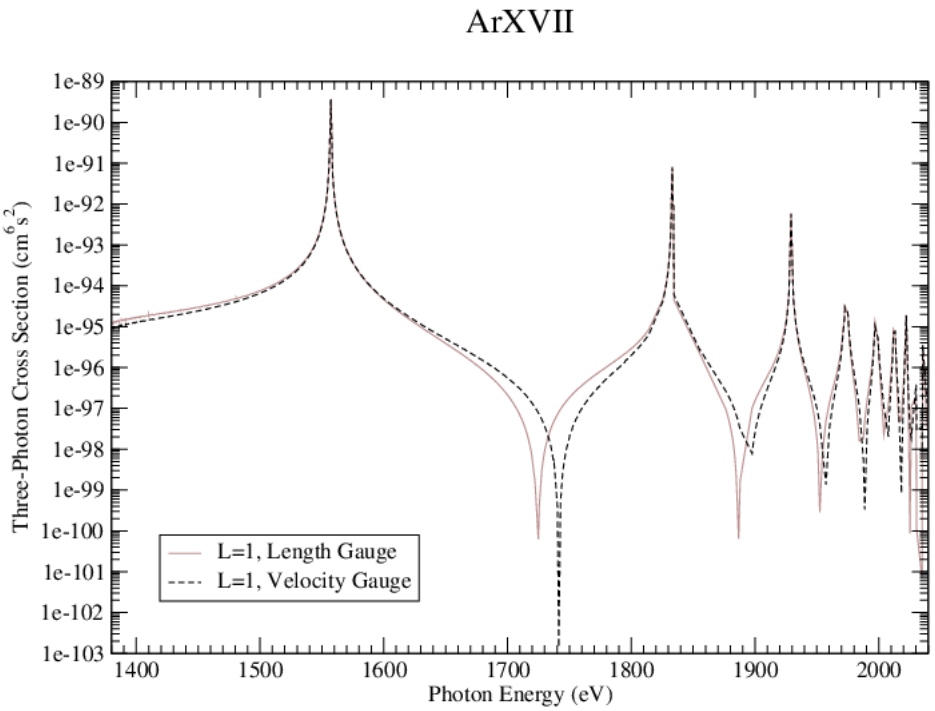

Figure 3.19: Three-photon, $L = 1$ ionization of Ar^{16+} in the 1380-2040 eV region, with $n_b = 170$ B-splines of order $k_b = 9$, 17 box-sizes R varied between $10 - 14.8$ $a.u.$, and 1600 included orbital configurations.

Table 3.19: Energy features of $Ar^{16+} \rightarrow Ar^{17+}$ three-photon, $L = 1$ cross section plot.

	Calculated eV		NIST eV	Discrepancy eV	Discrepancy %
		Ionization	4120.67		
1st Point	1368.91	$\hookrightarrow \div 3$	1373.56	4.65	0.3385
		$1s2s(^1S_0)$	3124.52		
1st Peak	1557.26	$\hookrightarrow \div 2$	1562.26	5.00	0.3200
		$1s3s(^1S_0)$	3679.46		
2nd Peak	1833.21	$\hookrightarrow \div 2$	1839.73	6.52	0.3544
		$1s3d(^1D_2)$	3683.59		
2nd Peak	1833.21	$\hookrightarrow \div 2$	1841.80	8.59	0.4664
		$1s4s(^1S_0)$	3873.03		
3rd Peak	1929.11	$\hookrightarrow \div 2$	1936.52	7.41	0.3826
		$1s4d(^1D_2)$	3874.76		
3rd Peak	1929.11	$\hookrightarrow \div 2$	1937.38	8.27	0.4269
		$1s5s(^1S_0)$	3962.41		
4th Peak	1972.64	$\hookrightarrow \div 2$	1981.21	8.57	0.4326
		$1s5d(^1D_2)$	3963.30		
4th Peak	1972.64	$\hookrightarrow \div 2$	1981.65	9.01	0.4547
		$1s6s(^1S_0)$	[no data]		
5th Peak	1996.95	$\hookrightarrow \div 2$	[N/A]	[N/A]	[N/A]
		$1s6d(^1D_2)$	[no data]		
5th Peak	1996.95	$\hookrightarrow \div 2$	[N/A]	[N/A]	[N/A]

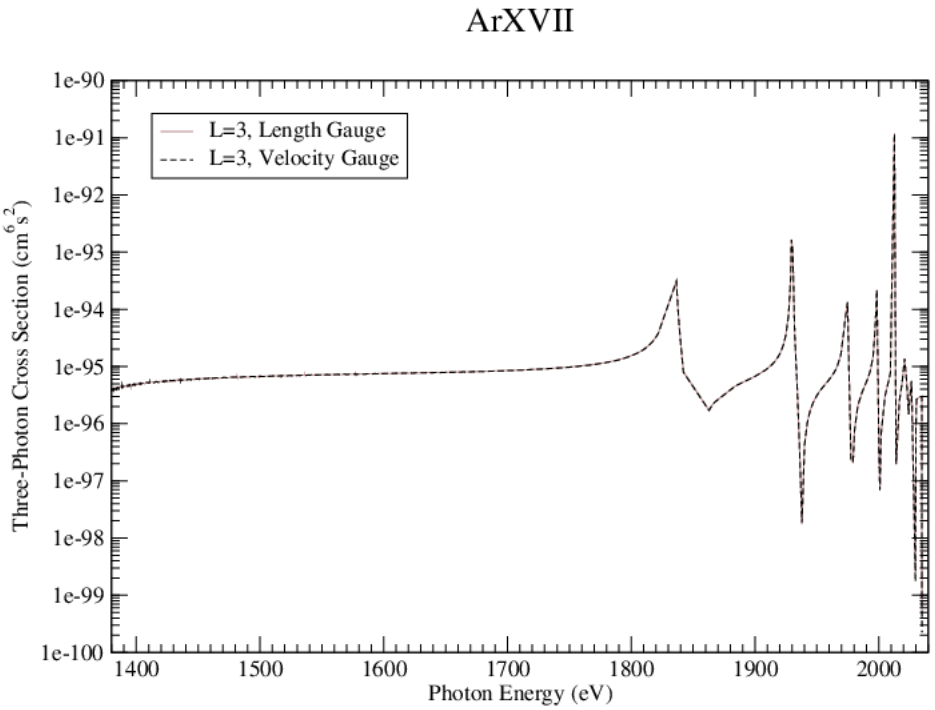

Figure 3.20: Three-photon, $L = 3$ ionization of Ar^{16+} in the 1380-2040 eV region, with $n_b = 170$ B-splines of order $k_b = 9$, 17 box-sizes R varied between $10 - 14.8$ $a.u.$, and 1600 included orbital configurations.

Table 3.20: Energy features of $Ar^{16+} \rightarrow Ar^{17+}$ three-photon, $L = 3$ cross section plot.

	Calculated eV		NIST eV	Discrepancy eV	Discrepancy %
		Ionization	4120.67		
1st Point	1368.90	$\hookrightarrow \div 3$	1373.56	4.66	0.3393
		$1s3d(^1D_2)$	3683.59		
1st Peak	1836.50	$\hookrightarrow \div 2$	1841.80	5.30	0.2878
		$1s4d(^1D_2)$	3874.76		
2nd Peak	1929.45	$\hookrightarrow \div 2$	1937.38	7.93	0.4093
		$1s5d(^1D_2)$	3963.30		
3rd Peak	1974.82	$\hookrightarrow \div 2$	1981.65	6.83	0.3447
		$1s6d(^1D_2)$	[no data]		
4th Peak	1998.48	$\hookrightarrow \div 2$	[N/A]	[N/A]	[N/A]

3.4 General Discussion

By comparing the cross section baselines (non-resonant regions) of the two and three photon cross sections, it is evident that the atoms/ions with a higher atomic number (Z) have a lower cross section by orders of magnitude (compared to the other atoms/ions of the same N-photon process). For the one-photon cross sections it is also true that the higher Z atoms/ions have lower cross sections (but the difference isn't orders of magnitude).

Chapter 4

Conclusions and Future Work

Calculations of one-, two- and three-photon partial ionization cross sections have been presented of the following helium-like atoms/ions: He, Li^{+}, Ne^{8+} and Ar^{16+}. This was achieved using the lowest-order perturbation theory for the electric field and an ab-initio code using a configuration-interaction method for the atomic structure calculations. The two-electron states were obtained by an expansion of a one-electron state basis, expressed with a set of non-orthogonal B-spline polynomials limited to a finite atomic radius (a "box size"). These calculations were performed with two different gauges to express the dipole matrix elements: the length gauge and velocity gauge, and generally, the results of both closely matched, granting a degree of confidence. Many test calculations were carried out with various combinations of atomic radii with considered electron configuration states, and ultimately, for each species, the data of 17 runs of code with varying atomic radii (with the same set of considered configuration states) was combined to produce the cross sections presented in this thesis.

The energies of a selection of one- and two-electron states have been tabulated for each species, taken from a run of the code of one sample atomic radius (the lowest box-size, in each case). These tabulated energies have been compared with the NIST atomic spectra database, with agreeable results, but a negative shift and a trend of increasing discrepancy with decreasing energy state has been observed. The one-electron state discrepancies have been noted to do with the number of computational grid points around the nucleus, and

that this could be improved by increasing the density of computational grid points in this region (by increasing the number of B-splines or changing the knot point distribution). The two-electron state discrepancies have been noted to do with the configuration interaction method, and they can be improved by increasing the number of included considered two-electron states.

The presented cross sections were examined and described, noting the interference patterns, and the positions (energy occurrences) of various energy features, namely the highest points of peaks and the first data point, were tabulated. It has been found that their cross sections are dominated by a series of intermediate (one- or two-photon) resonance peaks as well as by two-electron excitation autoionizing resonances. The specific resonance nature (energy state) of the peaks were identified, and compared with energy transitions and ionization energies from the NIST atomic spectra database, and matched up via tabulation, with generally agreeable comparisons, with energy shifts often accounted for by the two-electron state discrepancies.

These cross section calculations have been compared with the modelling and experiments of others, where available, producing generally agreeable results. Further comparisons could be made with future experiments, stimulated by the recent developments of light sources, notably FELs. In particular, the development of variable gap undulators (which permit straightforward tuning of the FEL wavelength) allow comparisons at a range of photon energies. This work could inspire one- and two-photon (or even three-, if possible) cross section experiments specifically on the species presented in this work, for example Li^{+}, Ne^{8+} and Ar^{16+}.

The general trend of the decreasing of cross sections with increasing Z of the target has been noticed, as well as the decreasing of cross sections with increasing N-photon process. For the two-photon processes, it has been observed that the ^1D ($L = 2$) channel overwhelms the ^1S ($L = 0$) one. All of the above trends are in accordance with the known properties of multiphoton atomic cross sections, either theoretically calculated or experimentally measured.

The cross sections could be enhanced further, including optimization of specific photon

energy regions (for example, the higher energy region of Ne^{8+}) to compare better with experiment. The cross sections could also be convolved, with relevant FEL bandwidths, making their comparison with experiment easier. Such examples of convolution data for the specific experiments go beyond the purposes of the present study. The cross sections made available here can be used in conjunction with the particular experimental conditions for realistic predictions of photoionization yields.

The photon energy scale could be converted to liberated electron energy: this would make them easier to compare with experiments that measure detected electron energy, and it would eliminate energy shift discrepancies due to discrepancy in ground state energy calculation. Additionally, further tests could be done on one-photon cross sections, for example on a range of helium-like species of varying atomic number from Li^+ to Ne^{8+} (or even to Ar^{16+}), to investigate if the odd curve at the start of the Ne^{8+} and Ar^{16+} cross sections are physical.

This work has only considered linearly polarized light, and so the calculations could be expanded to account for arbitrary light-polarization which some current and future planned FELs can produce.

Note to reader: a paper [51] was published presenting the more novel aspects of this work, namely the two- and three-photon cross sections of Li^+, Ne^{8+} and Ar^{16+}.

Bibliography

[1] F. H. M. Faisal. Theory of Multiphoton Processes, chapter The Perturbation theory, page 50. Springer Science + Business Media, New York, 1987.

[2] P. Kruit, J. Kimman, H. G. Muller, and M. J. van der Wiel. Electron spectra from multiphoton ionization of xenon at 1064, 532, and 355 nm. Phys. Rev. A, 28:248, 1983.

[3] J. B. West. Photoionisation of atomic ions. J. Phys. B, 34:45, 2001.

[4] J.B. West. Photoionisation cross sections of atomic ions. Radiat. Phys. Chem., 70:275, 2004.

[5] H. Kjeldsen. Photoionization cross sections of atomic ions from merged-beam experiments. J. Phys. B, 39, 2006.

[6] B. M. Johnson, M. Meron, A. Agagu, and K. W. Jones. Atomic physics and synchrotron radiation: The production and accumulation of highly charged ions. Nucl. Instr. Meth. Phys. Res. B, 24:391, 1987.

[7] L. Bex. Review of latest developments of ions sourcesnt. In Third European Particle Accelerator Conference, EPAC 92, pages 252–256. HAL, 1992.

[8] H. Winick and G. P. Williams. Overview of synchrotron radiation sources world-wide. Synchrotron Radiation News, 4:23, 1991.

[9] S. Schippers and et al. Photoionisation of ions with synchrotron radiation: from ions in space to atoms in cages. Contemporary Physics, 2015.

[10] C. Pellegrini. X-ray free-electron lasers: from dreams to reality. Phys. Scr., 169:014004, 2016.

[11] T. Tanaka. Current status and future perspectives of accelerator-based x-ray light sources. J. Opt., 19:093001, 2017.

[12] T. Glover, M. P. Hertlein, S. H. Southworth, T. K. Allison, J. van Tilborg, E. P. Kanter, B. Krassig, H. R. Varma, B. Rude, R. Santra, and et al. Controlling x-rays with light. Nat. Phys., 6:69, 2010.

[13] K. Tamasaku and et al. Double core-hole creation by sequential attosecond photoionization. Phys. Rev. Lett., 111:043001, 2013.

[14] M. Meyer, D. Cubaynes, V. Richardson, J. T. Costello, P. Radcliffe, W. B. Li, S. Dusterer, S. Fritzsche, A. Mihelic, K. G. Papamihail, P. Lambropoulos, and et al. Two-photon excitation and relaxation of the 3d-4d resonance in atomic kr. Phys. Rev. Lett., 104:213001, 2010.

[15] Y. H. Jiang, A. Rudenko, M. Kurka, and et al. Euv-photon-induced multiple ionization and fragmentation dynamics: From atoms to molecules. J. Phys. B, 42:134012, 2009.

[16] L. Young and et al. Femtosecond electronic response of atoms to ultra-intense x-rays. Nature, 466:56, 2010.

[17] H. Fukuzawa and et al. Deep inner-shell multiphoton ionization by intense x-ray free-electron laser pulses. Phys. Rev. Lett., 110:173005, 2013.

[18] V. Richardson, J. T. Costello, and et al. Two-photon inner-shell ionization in the extreme ultraviolet. Phys. Rev. Lett., 105:013001, 2010.

[19] J. Costello, E. Kennedy, and L.A.A. Nikolopoulos. Short wavelength free electron lasers. J. of Modern Optics, 63:285–287, 2016.

[20] C. Pellegrini, A. Marinelli, and S. Reiche. The physics of x-ray free-electron lasers. Rev. Mod. Phys., 88:015006, 2016.

[21] C. Bostedt, S. Boutet, D.M. Fritz, Z. Huang, H.J. Lee, H.T. Lemke, A. Robert, W.F. Schlotter, J.J. Turner, and G.J. Williams. Linac coherent light source: The first five years. Rev. Mod. Phys., 88:015007, 2016.

[22] R. Falcone, M. Dunne, H. Chapman, M. Yabashi, and K. Ueda. Frontiers of free-electron laser science ii. J. Phys. B, 49:180201, 2016.

[23] J. S. Parker, L. R. Moore, K. J. Meharg, D. Dundas, and K. T. Taylor. Double-electron above threshold ionization of helium. J. Phys. B, 34:69, 2001.

[24] L. R. Moore, M. A. Lysaght, L. A. A. Nikolopoulos, J. S. Parker, H. W. van der Hart, and K. T. Taylor. The rmt method for many-electron atomic systems in intense short-pulse laser light. J. of Modern Optics, 58:1132, 2011.

[25] L. A. A. Nikolopoulos and P. Lambropoulos. Multichannel theory of two-photon single and double ionization of helium. J. Phys. B, 34:545, 2001.

[26] L. A. A. Nikolopoulos. Mg in electromagnetic fields: Theoretical partial multiphoton cross sections. Phys. Rev. A, 71:033409, 2005.

[27] S W Scully, I Alvarez, C Cisneros, and et al. Doubly excited resonances in the photoionization spectrum of li^+: experiment and theory. J. Phys. B, 39:3957–3968, 2006.

[28] T.N. Chang and Y.S. Kim. Theoretical study of the two-electron interaction in alkaline-earth atoms. Phys. Rev. A, 34:2609, 1986.

[29] X. Tang, T.N. Chang, P. Lambropoulos, S. Fournier, and L.F. DiMauro. Multiphoton ionization of magnesium with configuration-interaction calculations. Phys. Rev. A, 41:R5265, 1990.

[30] T.N. Chang and X. Tang. Photoionization of two-electron atoms using a nonvariatonal configuration interaction approach with discretized finite basis. Phys. Rev. A, 44:232–238, 1991.

[31] T.N. Chang. Many-body theory of Atomic Structure, chapter B-spline based Configuration-Interaction Approach for Photoionization of Two-electron and Divalent Atoms, pages 213–247. World Scientific, Singapore, 1993.

[32] L. A. A. Nikolopoulos. A package for the ab-initio calculation of one- and two-photon cross sections of two-electron atoms, using a ci b-splines method. Comput. Phys. Commun., 150:140–165, 2003.

[33] Carl de Boor. A Practical Guide to Splines. Springer - Verlag, New York, 1978.

[34] I. Sobel'man. Introduction to the theory of atomic spectra. Pergamon Press Ltd, Oxford, 1972.

[35] A. Kramida, Yu. Ralchenko, J. Reader, and and NIST ASD Team. NIST Atomic Spectra Database (ver. 5.3), [Online]. Available: `http://physics.nist.gov/asd` [2016, June 19]. National Institute of Standards and Technology, Gaithersburg, MD., 2015.

[36] L. A. A. Nikolopoulos and P. Lambropoulos. Above-threshold ionization of negative hydrogen. Phys. Rev. A, 56:3106, 1997.

[37] P. Lambropoulos. Topics on multiphoton processes in atoms. Adv. At. Mol. Opt. Phys., 12:87, 1976.

[38] T.N. Chang. Widths of the doubly excited resonances of the two-electron atoms below the n=2 threshold. Phys. Rev. A, 47:705, 1993.

[39] J. B. West and G. V. Marr. The absolute photoionization cross sections of helium, neon, argon and krypton in the extreme vacuum ultraviolet region of the spectrum. Proc. R. Soc. Lond., 349:397, 1976.

[40] D A Verner, G J Ferland, and K T Korista. Atomic data for astrophysics. ii. new analytic fits for photoionization cross section of atoms and ions. Astrophys. J., 465:487–498, 1996.

[41] K. L. Bell and A. E. Kingston. Photoionization cross sections for the helium isoelectronic series. J. Phys. B, 4:1308, 1971.

[42] Takahiro Sato and et al. Determination of the absolute two-photon ionization cross section of he by an xuv free electron laser. J. Phys. B, 44:161001, 2011.

[43] H. W. van der Hart, B. J. S. Doherty, J. S. Parker, and K. T. Taylor. Benchmark multiphoton ionization rates for he at 390 nm. J. Phys. B, 38:207, 2005.

[44] A Emmanouilidou, V Hakobyan, and P Lambropoulos. Direct three-photon triple ionization of li and double ionization of li+. J. Phys. B, 46:111001, 2013.

[45] S A Novikov and A N Hopersky. Two-photon excitation-ionization of the 1s shell of highly charged positive atomic ions. J. Phys. B, 34:4857–4863, 2001.

[46] G Doumy, C Roedig, and et al. Nonlinear atomic response to intense ultrashort x rays. Phys. Rev. Lett., 106:083002, 2011.

[47] A Sytcheva, S Pabst, S Son, and R Santra. Enhanced nonlinear response of ne8+ to intense ultrafast x rays. Phys. Rev. A, 85:023414, 2012.

[48] P. Koval. Two-photon ionization of atomic inner-shells. PhD thesis, Univ. Kassel, 2004.

[49] T. Laarmann and et al. Photoionization of helium atoms irradiated with intense vacuum ultraviolet free-electron laser light. part i. experimental study of multiphoton and single-photon processes. Phys. Rev. A, 72:023409, 2005.

[50] L. A. A. Nikolopoulos. Unpublished notes.

[51] W. Hanks, J. T. Costello, and L. A. A. Nikolopoulos. Two- and three-photon partial photoionization cross sections of li^{+}, ne^{8+} and ar^{16+} under xuv radiation. Appl. Sci., MDPI, 7:294, 2017.